J. Fluid Mech. (2007), *vol.* 573, *pp.* 339–369.
doi:10.1017/S0022112006003909 Printed in the United Kingdom

Vortices in oscillating spin-up

M. G. WELLS†, H. J. H. CLERCX AND G. J. F. VAN HEIJST

Department of Applied Physics, Eindhoven University of Technology,
PO Box 513, NL-5600 MB Eindhoven, The Netherlands

(Received 30 August 2005 and in revised form 18 August 2006)

Laboratory experiments and numerical simulations of oscillating spin-up in a square tank have been conducted to investigate the production of small-scale vorticity near the no-slip sidewalls of the container and the formation and subsequent decay of wall-generated quasi-two-dimensional vortices. The flow is made quasi-two-dimensional by a steady background rotation, and a small sinusoidal perturbation to the background rotation leads to the periodic formation of eddies in the corners of the tank by the roll-up of vorticity generated along the sidewalls. When the oscillation period is greater than the time scale required to advect a full-grown corner vortex to approximately halfway along the sidewall, dipole structures are observed to form. These dipoles migrate away from the walls, and the interior of the tank is continually filled with new vortices. The average size of these vortices appears to be largely controlled by the initial formation mechanism. Their vorticity decays from interactions with other stronger vortices that strip off filaments of vorticity, and by Ekman pumping at the bottom of the tank. Subsequent interactions between the weaker 'old' vortices and the 'young' vortices result in the straining, and finally the destruction, of older vortices. This inhibits the formation of large-scale vortices with diameters comparable to the size of the container.

The laboratory experiments revealed a $k^{-5/3}$ power law of the energy spectrum for small-to-intermediate wavenumbers. Measurements of the intensity spectrum of a passive scalar were consistent with the Batchelor prediction of a k^{-1} power law at large wavenumbers. Two-dimensional numerical simulations, under similar conditions to those in the experiments (with weak Ekman decay), were also performed and the simultaneous presence of a $k^{-5/3}$ and $k^{-3-\zeta}$ (with $0 < \zeta \ll 1$) power spectrum is observed, with the transition occurring at the wavenumber at which vorticity is injected from the viscous boundary layer into the interior. For higher Ekman decay rates, steeper spectra are obtained for the large wavenumber range, with $\zeta = O(1)$ and proportional to the Ekman decay rate. Movies are available with the online version of the paper.

1. Introduction

Laboratory experiments of oscillating spin-up of rotating fluids in square containers and direct numerical simulations of two-dimensional oscillating spin-up in square domains with no-slip boundaries have been conducted. With this experimental technique, which enables continuous generation of vortices in a confined area (even with the possibility of varying the bottom drag by changing the water depth), we

† Present address: Department of Physical and Environmental Sciences, University of Toronto, 1265 Military Trail Road, Toronto, Ontario M1C 1A4, Canada.

investigate the production of small-scale vorticity near the no-slip sidewalls of the container and the formation and subsequent decay of wall-generated quasi-two-dimensional vortices. The decay of the vortices is due to the interaction with other strong vortices (vortex stripping) and to the effects of Ekman pumping at the bottom of the tank, thus preventing the formation of large-scale vortices with diameters comparable to the container size. Additionally, two-dimensional numerical simulations of oscillating spin-up have been carried out in order to assess the small-scale vorticity production (which is not possible in the experiments), to vary bottom friction (used to model Ekman pumping), to distinguish between vortex stripping and Ekman pumping as the dominant decay mechanism of the vortices, and to explore a different parameter range from that accessible with the experiments.

In the laboratory experiments, the flow is made quasi-two-dimensional by a steady background rotation. A small sinusoidal perturbation to the background rotation leads to the periodic formation of eddies in the corners of the tank by the roll-up of vorticity generated along the sidewalls. When the oscillation period is greater than the time scale required to advect a full-grown corner vortex to approximately halfway along the sidewall, dipole structures are observed to form. These dipoles migrate away from the walls and fall apart into separate vortices owing to interaction with other vortices. The interior of the tank is thus continually filled with new vortices. After certain forcing periods, a sea of vortices emerges in the interior of the tank. In the present experiment, the production of small-scale vorticity, the subsequent formation of vortices, and some aspects of the evolution of this system of continuously interacting vortices are investigated. Moreover, although not pursued in the present experiments, the set-up allows investigation of the role of bottom drag, which can be varied systematically, and the study of the interaction of this confined system of vortices with the lateral no-slip boundaries.

An important effect of no-slip boundaries on the evolution of a (turbulent) flow field is that if there is a continued input of energy into the system, then dissipation at the boundaries naturally occurs and the kinetic energy of the flow does not grow without limit. Thus, in a numerical simulation, a quasi-steady state for the kinetic energy of the flow can be reached without the introduction of additional sinks such as Rayleigh damping to dissipate the kinetic energy. Secondly, the injection of filaments of vorticity and small vortices (after the roll-up of the viscous boundary layers) represents a source of vorticity whose scale is independent of the forcing scale itself, but depends on the Reynolds number of the flow and the dimensionless forcing frequency (i.e. it depends on the thickness of the viscous Stokes boundary layer). In simulations of a decaying initial distribution of vortices, a similar source can clearly be seen in spectra where there is a change in the slope of the energy spectrum at the wavenumber corresponding to the thickness of the viscous boundary layer, k_δ. For $k < k_\delta$, the spectrum is characterized by a $k^{-5/3}$ range, characteristic of the inverse energy cascade, and for $k > k_\delta$ there is a k^{-3} range observed in the kinetic energy spectrum, characteristic of the direct enstrophy cascade (Clercx & van Heijst 2000).

The paper is organized as follows. In § 2, we describe a laboratory experiment that is able to inject vortices continuously from the boundary into the interior. Some simple scaling arguments are then presented to describe the initial size and strength of these vortices, as a function of the forcing parameters. Experimental observations of the formation of vortices and their properties are presented in § 3. In § 4, we discuss results obtained by a direct numerical flow simulation based on the two-dimensional Navier–Stokes equations in order to improve the understanding of the flow dynamics observed in the laboratory experiments. These numerical simulations complement

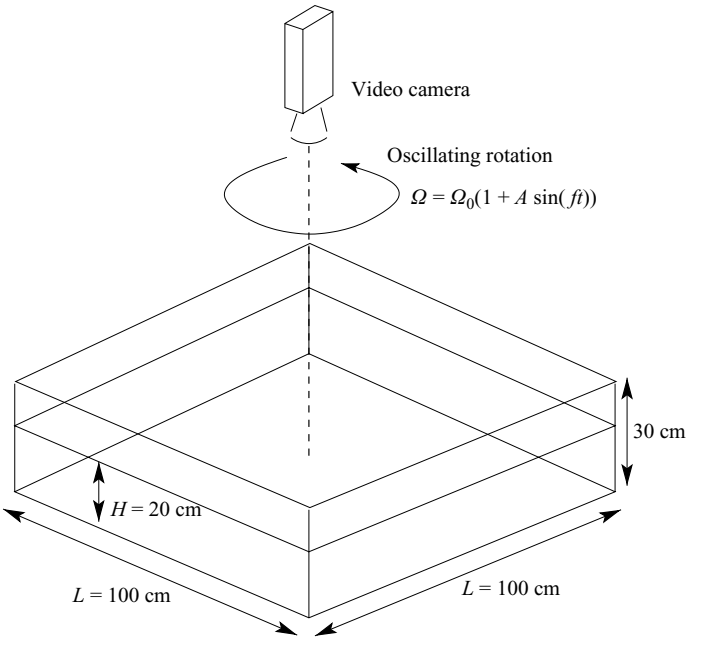

FIGURE 1. A sketch of the experimental set-up: a camera is mounted above the table and rotates in the same reference frame to record the movement of particles or dye. The tank has a half-width $L = 50$ cm and height of 30 cm. The fluid layer has a depth $H = 20$ cm. Typical rotation rates were 1 rad s^{-1}, with a fixed forcing amplitude $A\Omega_0 = 0.06$ rad s^{-1} and frequencies f in the range 0.031–0.126 rad s^{-1}.

the laboratory experiments, in which quantities such as vorticity, energy spectra and enstrophy are difficult to measure and in which it is difficult to explore the effects of large changes in the forcing parameters. Conclusions are summarized in § 5.

2. Experimental design

The laboratory experiments were performed in a tank of square cross-section, with dimensions $100 \times 100 \times 30\,\text{cm}^3$ (length × width × depth). This tank is mounted on a rotating table (see figure 1) and the flow is made quasi-two-dimensional by a steady background rotation of 1 rad s^{-1} to which a small sinusoidal perturbation is added:

$$\Omega(t) = \Omega_0(1 + A\sin(ft)), \tag{2.1}$$

where Ω_0 is the mean rotation rate, A is the (dimensionless) amplitude of the perturbation and f is the frequency. In a typical experiment, the tank is spun up from rest, and through the action of Ekman pumping the flow becomes quasi-two-dimensional after approximately 100 revolutions. The perturbation amplitude is $A = 0.06$ and the forcing frequency f is in the range 0.031–0.126 rad s^{-1}. The parameters of all the experiments that have been conducted are summarized in table 1.

Quasi-two-dimensional flows as found in the present experiments and the two-dimensional numerical simulations are characterized by three dimensionless numbers (see also § 4): the Reynolds number; the dimensionless forcing frequency $\mathscr{F} = f/A\Omega_0$; and the dimensionless Ekman decay rate. Alternatively, one might use the Rossby and Ekman numbers and again $\mathscr{F}$. However, keeping in mind the emphasis in the present investigation on the role of lateral boundary layers and decay by Ekman pumping,

Experiment	A	f (rad s^{-1})	$\mathscr{F}$	Re	α/f
1	0.06	0.031	0.52	15 000	0.161
2	0.06	0.063	1.05	15 000	0.079
3	0.06	0.094	1.57	15 000	0.053
4	0.06	0.126	2.09	15 000	0.040

TABLE 1. A summary of all the parameters used in the experiments conducted in a $100 \times 100\,\mathrm{cm}^2$ tank. All experiments reported had a water depth of 20 cm and a mean rotation rate of $\Omega_0 = 1\,\mathrm{rad\,s}^{-1}$. The Reynolds number is defined by $Re = UL/\nu = A\Omega_0 L^2/\nu$, with $\nu = 1 \times 10^{-2}\,\mathrm{cm}^2\,\mathrm{s}^{-1}$. The tank half-width $L = 50$ cm is used for consistency with the numerical simulations.

the former set of dimensionless numbers is most appropriate. From the definition of the dimensionless frequency, we can conclude that there is no need to vary f, A and Ω_0 independently, but we should vary $\mathscr{F}$ alone. In the present study we have fixed A and Ω_0, with the condition that the flow should behave quasi-two-dimensionally in the geostrophic interior, and we varied only the forcing frequency f.

In the rotating frame of reference, the fluid oscillates back and forth around the axis of the tank. A similar set-up, with a slightly different forcing of the fluid in a rectangular container, was used in experiments by van Heijst (1989) and van de Konijnenberg *et al.* (1994) where the rotation rate Ω_0 of a fluid spinning in solid-body rotation was suddenly increased with an amount $\Delta\Omega_0$. In the rotating frame of reference (with angular velocity $\Omega_0 + \Delta\Omega_0$), this is equivalent to suddenly changing the relative vorticity of the flow by an amount $\delta\omega = -2\Delta\Omega_0$. In this case, an anticyclonic flow arises in the tank with maximum velocities along the sidewalls. Similar phenomena are observed in the present experiment, in which the background rotation rate is changed continuously. In this case the maximum flow velocity, its absolute value denoted by U, occurs near the sidewalls of the tank and scales with $(\Omega(t) - \Omega_0) \times L$ so that $U = A\Omega_0 L$, where L is the half-width of the tank. The oscillation acts to provide a forcing to the vorticity field: the overall relative vorticity changes as $\delta\omega = -2A\Omega_0 \sin(ft)$ in the rotating frame of reference.

The induced oscillating flow in the tank is strongly affected by the vertical sidewalls, which imply the presence of viscous boundary layers that contain high-amplitude vorticity. Near the corners of the tank, the flow may separate and the vorticity produced in the boundary layer will accumulate in the eddies emerging near the corners, as observed by van Heijst (1989) and van Heijst, Davies & Davis (1990) for spin-up flows. These eddies increase in radius with time as the vorticity produced in the viscous boundary layers is continuously advected toward the corners. The size and strength of the eddies is affected by both the strength of the vorticity in the boundary layer (or, stated differently, by the boundary-layer thickness), and by the time in which the vortex is able to form. Thus as the amplitude of the sinusoidal forcing $A\Omega_0$ is decreased, or the frequency f is increased beyond a certain threshold value (to be determined later on), weaker or no vortices will form in the corners of the tank. In experiments with an oscillating flow, on every forcing cycle, vortices will be formed in the corners of the tank. When the forcing changes direction, newly formed vortices detach from the corners and travel with the mean flow. These vortices usually travel approximately halfway along the sidewall, thereby promoting the detachment and roll-up of the boundary layer. This process results in the formation of opposite-signed vortices, resulting in the generation of vortex dipoles. It should

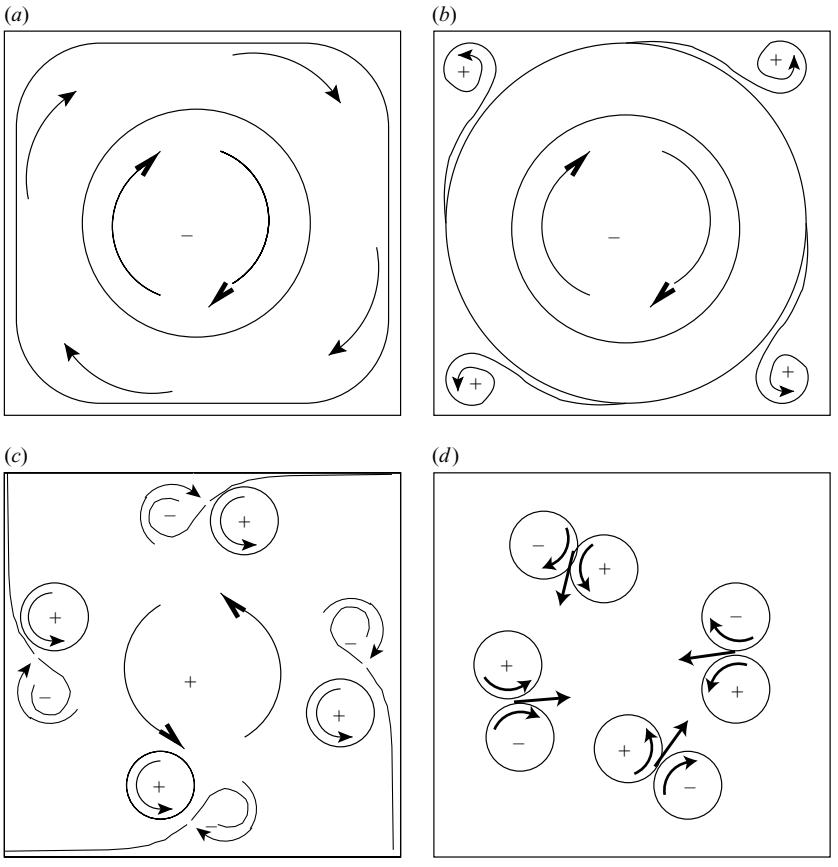

FIGURE 2. A schematic cartoon of the formation of dipolar structures in the oscillating flow. (*a*) Initially the interior flow can be described as having uniform negative vorticity (−). (*b*) The no-slip boundaries lead to the accumulation of positive (+) vorticity in each of the corners resulting in four vortices. These vortices are then advected by the flow as the forcing changes sign (*c*), and can form dipolar structures by pairing with the negative vortices. These dipoles can then self-propagate into the interior (*d*).

be mentioned that, for convenience, we assume the formation of dipoles just halfway along the sidewalls. From the simulations, it can be concluded that this is a realistic assumption for the range $2000 \leqslant Re \leqslant 10\,000$. The low-Reynolds-number simulations, however, show dipole formation in the corners of the tank whereas the high-Reynolds-number simulations indicate that dipole formation can occur much more rapidly and frequently. This has no consequences for the scaling laws to be derived later on, except for slightly different constants of proportionality. Dipoles are able to move by self-propagation, so they will move away from the boundaries and thereby fill the interior with a field of quasi-two-dimensional (columnar) vortices (figure 2). The remaining part of the boundary layer is advected to the corner of the domain to form the next corner vortex, so that the process of dipole formation can continue.

The mechanism can be understood by observations of movies from numerical simulations (an animation of the vorticity field is available as a supplement to the online version of the paper). Note that while there is a fourfold rotation symmetry inherently related to the forcing protocol, small perturbations always result in a symmetry breaking of the flow field.

Dipoles can be formed in experiments when the time required for a newly formed vortex to be advected approximately halfway along the sidewall is less than half a forcing period. The time scale for advection along one side of the tank over a length L, with a mean velocity

$$\bar{U} = \frac{f}{\pi}\int_0^{\pi/f} A\Omega_0 L \sin(ft)\,\mathrm{d}t = 2U/\pi,$$

will be $\tau = L/\bar{U} = \pi/(2A\Omega_0)$. If this time scale is less than half the oscillation period $T = 2\pi/f$, then a vortex travelling along the side will be able to detach and roll up a sufficient part of the boundary layer to form an opposite-signed vortex. Hence, dipoles form if

$$\frac{f}{A\Omega_0} = \mathscr{F} < 2. \tag{2.2}$$

The actual threshold for dipole formation occurs at a slightly lower value of $\mathscr{F}$ (for the experiments with $Re = 15\,000$ the threshold is found for $\mathscr{F} \approx 1.7$; this value is also supported by numerical data from two-dimensional simulations, see § 4.1). A gradual transition is expected to exist between the regimes where dipoles are formed ($\mathscr{F} \lesssim 1.5$), and where they are not formed ($\mathscr{F} \gtrsim 2$).

The Reynolds number of the forcing is defined as

$$Re = \frac{UL}{\nu} = \frac{A\Omega_0 L^2}{\nu}, \tag{2.3}$$

where $U = A\Omega_0 L$, and ν is the kinematic viscosity of the fluid. For typical laboratory experiments, $Re \approx 15\,000$. This Reynolds number should not be confused with the micro-scale Reynolds number based upon the ratio of the circulation $|\Gamma_v|$ of the vortices to the molecular viscosity ν, defined as $Re_m = |\Gamma_v|/\nu$. As the total circulation in a bounded flow must be zero, the changes in uniform interior vorticity owing to the variable rotation rate must be balanced by thin layers with strong vorticity of the opposite sign that eventually accumulate partly in the corner vortices. Approximately half of the vorticity in the boundary layer is advected to the corners, the other half has already been injected into the interior as part of the dipoles. Thus, the circulation $|\Gamma_v|$ in each of these four corner vortices will be one-eighth of the magnitude of the circulation corresponding to the uniform vorticity over the tank, averaged over half the forcing cycle, or

$$|\Gamma_v| = \frac{f}{\pi}\int_0^{\pi/f} A\Omega_0 L^2 \sin(ft)\,\mathrm{d}t = \frac{2}{\pi} A\Omega_0 L^2. \tag{2.4}$$

This implies that initially $Re_m \simeq 0.6Re$. However, the dissipation during the advection of vorticity from the thin boundary layer, containing steep vorticity gradients, will eventually result in weaker vortices than expected. Subsequent interactions between vortices and damping processes (lateral diffusion, Ekman damping) will often yield values much smaller than Re for the individual vortices. In our experiments (with $Re \approx 15\,000$), initial values of Re_m were measured as high as 8000 (consistent with $Re_m \simeq 0.6Re \approx 9000$), with the older vortices having lower values, $Re_m \sim O(10^2 - 10^3)$.

2.1. *Scaling of the size and strength of the corner vortices*

The size of the vortices constituting these dipoles can be estimated by considering the input of vorticity from the Stokes boundary layer through one half of the forcing cycle. A crude estimate of the boundary-layer thickness δ can be made (see, e.g.

Kundu 1990),

$$\delta \approx \pi\sqrt{\frac{2\nu}{f}}, \tag{2.5}$$

so that the dimensionless boundary-layer thickness scales as $\delta/L \approx \pi\sqrt{2/Re\mathscr{F}}$.

It will be assumed that the vortex grows by advection of the boundary-layer vorticity and the subsequent roll-up of the detached vorticity filament. The area occupied by the vortex (radius ρ) after half a forcing cycle is approximately $\pi\rho^2 \approx L\delta$. Using the definition of the Reynolds number, (2.3), the radius of the vortices formed in the corners of the container will scale as

$$\frac{\rho}{L} \approx \left(\frac{2}{Re\mathscr{F}}\right)^{1/4} \simeq 1.19 Re^{-1/4}\mathscr{F}^{-1/4}. \tag{2.6}$$

Provided the experiment is in the regime where dipoles can form, i.e. $\mathscr{F} \lesssim 1.5$, then (2.6) provides an estimate of the scale of the vortices injected (as a part of the dipoles) into the interior.

The relative strengths of the vortices can be estimated from the fact that in a bounded domain with stationary no-slip walls the circulation Γ for the domain $\mathscr{D}$ must be zero. All the vorticity in the small vortices created after half a forcing cycle, with total area $\pi\rho^2$, must balance the (lower) vorticity, averaged over half the forcing cycle, in the rest of the tank. As a first-order approximation, we assume a parabolic vorticity distribution in the vortices of the form $\omega(r) = \omega_{max}(1 - (r/\rho)^2)$ for $r \leqslant \rho$ (with ω_{max} the amplitude of the vortex) and zero elsewhere. The circulation of such a vortex is $|\Gamma_v| = \frac{1}{2}\pi\rho^2|\omega_{max}| = (2/\pi)A\Omega_0 L^2$, where the latter equality results from applying (2.4). The vorticity in the corner vortices, $|\omega_{max}|$, and hence the vorticity of the boundary layers, should thus scale as

$$\frac{|\omega_{max}|}{A\Omega_0} \approx \frac{2\sqrt{2}}{\pi^2}\sqrt{Re\mathscr{F}} \simeq 0.29\sqrt{Re\mathscr{F}}. \tag{2.7}$$

To summarize, as the Reynolds number or the dimensionless forcing frequency (provided $\mathscr{F} \lesssim 1.5$) is increased, the vortices decrease in size (2.6) and increase in strength (2.7).

The numerical validation of relations (2.6) and (2.7), to be discussed in § 4 (the simulations without bottom friction), reveal that

$$\frac{\rho_{mean}}{L} \approx 1.5 Re^{-1/4}\mathscr{F}^{-1/4}, \qquad \frac{|\omega_{mean}|}{A\Omega_0} \approx 0.23\sqrt{Re\mathscr{F}}, \tag{2.8}$$

thus with the same scaling as predicted by (2.6) and (2.7), but with slightly different constants of proportionality. Note that ω_{mean} is not exactly the same as ω_{max}; the former is an average obtained from numerical data as explained in § 4.3 and the latter is the maximum amplitude of the vortices. Necessarily, $|\omega_{mean}| \lesssim |\omega_{max}|$, owing to the effects of horizontal diffusion when vortices travel to the interior of the domain, although the same scaling with respect to Re and $\mathscr{F}$ is anticipated. Similarly, ρ_{mean} is an average and (2.8) indicates that $\rho_{mean} \gtrsim \rho_{max}$, as expected when again taking horizontal diffusion into account. The average vortex radius (ρ_{mean}) and vortex amplitude ($|\omega_{mean}|$) can thus be accurately predicted. One should, however, keep in mind that, in particular, the amplitude of the vortices in the experiments have decreased substantially before they can be resolved experimentally owing to horizontal diffusion and, possibly, Ekman damping.

Three-dimensional effects arise in rotating flows owing to the presence of Ekman boundary layers at horizontal domain boundaries, which lead to Ekman pumping and decay of circulation in the vortices. The Ekman decay time scale is given by $T_E = H/\sqrt{\nu\Omega_0}$. A clear separation between the forcing period and the Ekman decay time scale requires that $T_E \gg 2\pi/f$. In the regime where dipoles form, $\mathscr{F} \lesssim 1.5$, the condition $Ro = U/(2\Omega_0 L) = A/2 \ll 1$ in order to have a quasi-two-dimensional flow, implies $T_E \gtrsim 2\pi/f$ (note that in the experiments discussed later in this paper $Ro = 0.03 \ll 1$). For example, in our experiments, the period of oscillation $2\pi/f$ is typically between 50 and 200 s, and a typical Ekman decay time scale is about 200 s (with $\Omega_0 = 1\,\mathrm{rad\,s^{-1}}$, $H = 0.20\,\mathrm{m}$ and $\nu = 10^{-6}\,\mathrm{m^2\,s^{-1}}$).

3. Laboratory results

The formation of dipoles in experiments with $\mathscr{F} \lesssim 1.5$ is most easily visualized by the rapid stirring of dye (figure 3). In this experiment, $f = 0.031\,\mathrm{rad\,s^{-1}}$ ($T = 200\,\mathrm{s}$), $A\Omega_0 = 0.06\,\mathrm{rad\,s^{-1}}$, so that $\mathscr{F} = 0.52$, corresponding with a regime in which strong dipole formation is expected. A small amount of fluorescein dye was initially injected near the bottom left-hand corner. After $t/T = 0.025$, the flow has sheared and stretched this dye blob along one wall of the tank, and several vortices have started to stir at smaller scales. A subsequent image at $t/T = 0.125$ (figure 3*b*) shows that the dye has been sheared around the complete perimeter of the tank, and two dipolar structures are beginning to transport dye into the interior. Once dye has reached the interior of the tank, it is rapidly mixed by the field of vortices. In figure 3(*c*), about 15 circular structures in the dye streaks can be observed, which indicate the presence of localized vorticity in the interior. These vortices result in almost complete mixing of the dye by $t/T = 0.325$ after its injection (figure 3*d*).

To understand the importance of the dipole formation process in determining the amount of mixing in the tank, it is useful to consider an experiment where strong dipoles did not form. The experiment illustrated in figure 4 had a forcing frequency of $f = 0.126\,\mathrm{rad\,s^{-1}}$, $A\Omega_0 = 0.06\,\mathrm{rad\,s^{-1}}$, so that $\mathscr{F} = 2.09$. Dye was injected into the flow in a similar manner to that in figure 3. After $t/T = 3.6$, the dye was well mixed around the perimeter of the tank, but the central portion of the container remained free of dye. Flow separation has still taken place in the corners, and the resulting vortices can be observed in the dye filaments, but because of the high oscillation frequency, these vortices were unable to form dipoles which could have rapidly left the wall region.

The images in figures 3 and 4 show that the size of these vortices is about 10–15 % of the width of the tank. In other experiments in which the parameters f and $A\Omega_0$ were changed systematically to modify the relevant dimensionless numbers Re and $\mathscr{F}$, qualitative agreement with (2.6), in that the vortex size decreases with increasing $\mathscr{F}$ and Re, has been observed. Because of difficulties in spanning a large range of forcing parameters and still maintaining a quasi-two-dimensional flow field in the laboratory experiments, a quantitative experimental comparison with the scaling relations (2.6) and (2.7) has not been made. Validation of these scaling relations will be based on numerical evidence (see § 4.2).

3.1. *Particle tracking*

During an experiment, the motion of tracer particles is monitored by a digital camera in order to determine the velocity field. The images are recorded onto a computer and after the experiment, the Lagrangian trajectories of the particles are

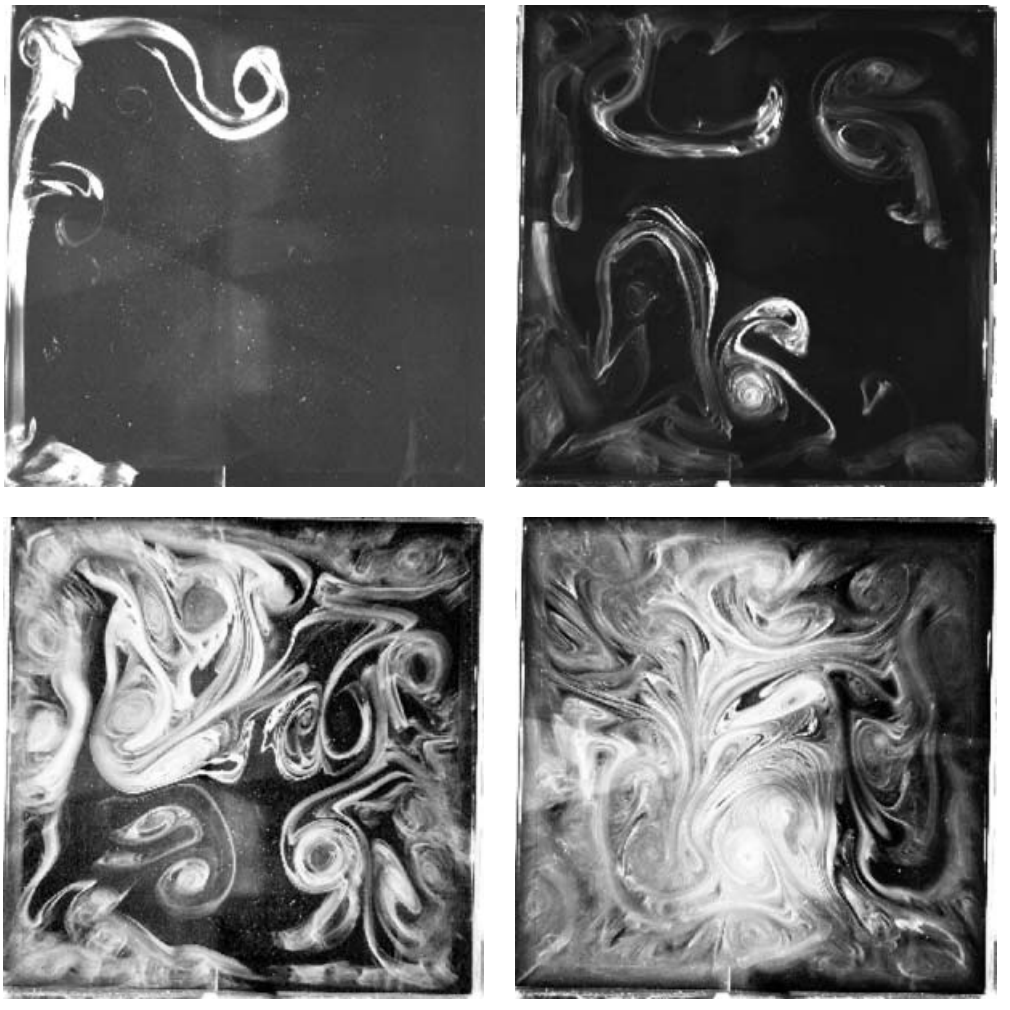

FIGURE 3. A sequence of laboratory photographs of a dye tracer showing the turbulent field of vortex structures. (*a*) $t/T = 0.025$ after dye has been injected in the corner of the tank, (*b*) $t/T = 0.125$, (*c*) $t/T = 0.175$, and (*d*) by $t/T = 0.325$ the dye has been well mixed in the tank, and the vortex structures are clearly visible. In this experiment $\mathscr{F} = 0.52$, $f = 0.031\,\mathrm{rad\,s^{-1}}$ (so that $T = 2\pi/f = 200\,\mathrm{s}$) and $Re = 15\,000$ (experiment 1, table 1). An animation of this experiment is available as a supplement to the online version of the paper.

determined using the particle-tracking algorithm developed by Bastiaans, van der Plas & Kieft (2002). An SMD-1M15 CCD camera with 1024×1024 pixels and 12 bit grey-scale resolution allowed high-quality images to be obtained at a rate of 5 frames per second. After using the particle-tracking algorithm, typically, 9000 particles could be tracked to allow interpolation of the velocity field to an 80×80 grid with about $1\,\mathrm{cm}^2$ resolution. Figures 5(*a*) and 5(*b*) show velocity vectors (indicating the streamlines) and vorticity contour plots from an experiment with $A\Omega_0 = 0.06\,\mathrm{rad\,s^{-1}}$ and $f = 0.031\,\mathrm{rad\,s^{-1}}$. This implies a forcing scale Reynolds number of $Re = 15\,000$ using (2.3) and a dimensionless frequency $\mathscr{F} = 0.52$. In figures 5(*a*) and 5(*b*), small individual vortices, with $|\omega_{mean}| \simeq 0.8$–$0.9\,\mathrm{s^{-1}}$ and $\rho/L \simeq 0.15$, are visible in the vorticity contour plots which are advected by the mean background flow. The observed

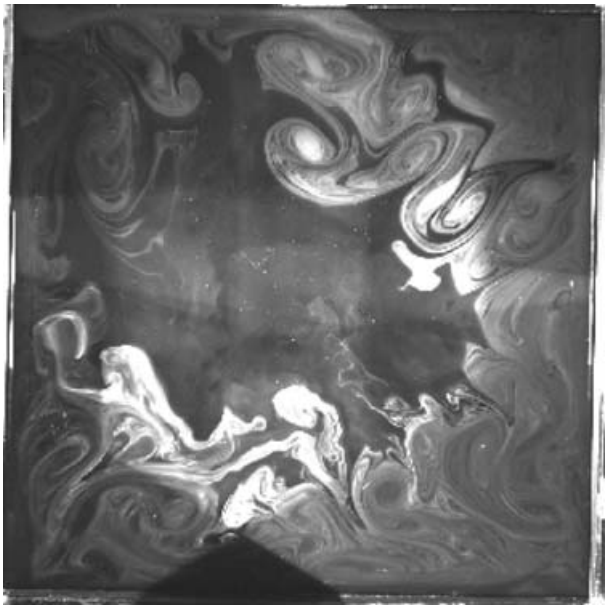

FIGURE 4. A photograph taken approximately four oscillation periods after dye has been released for an experiment with $\mathscr{F} = 2.09$ ($Re = 15\,000$, experiment 4, table 1). In contrast to the previous figure the dye is not well mixed and has been transported only around the perimeter of the tank. This is due to the forcing parameters having $\mathscr{F}$ sufficiently larger than unity so that dipoles could not form efficiently.

ratio $|\omega_{mean}|/A\Omega_0 \simeq 14$, somewhat smaller than the predicted ratio (2.8), which gives $|\omega_{mean}|/A\Omega_0 \simeq 20$. This is most probably due to the diminished separation between the forcing and Ekman time scales T and T_E, respectively, resulting in rapid decay of the vortices by Ekman pumping (see § 4.4). For these strongest vortices, the micro-scale Reynolds number can be estimated as

$$Re_m = |\Gamma_v|/\nu \approx \tfrac{1}{2}|\omega_{max}|\pi\rho^2/\nu = \frac{\pi}{2}\frac{|\omega_{max}|}{A\Omega_0}\left(\frac{\rho}{L}\right)^2 Re \simeq 8000,$$

in reasonable agreement with the prediction $Re_m \approx 0.6Re \simeq 9000$; the other weaker vortices visible in figure 5 would have $Re_m \sim 10^2$–10^3.

In figures 5(c) and 5(d), velocity vectors and vorticity contours from an experiment with $A\Omega_0 = 0.06\ \mathrm{rad\,s^{-1}}$ and a higher forcing frequency, $f = 0.094\ \mathrm{rad\,s^{-1}}$ (i.e. $\mathscr{F} = 1.57$) are shown. The peak vorticities shown in figure 5(d), namely, $|\omega_{mean}| \simeq 0.8\ \mathrm{s^{-1}}$ (or $|\omega_{mean}|/A\Omega_0 \simeq 13$), are smaller than predicted by the ratio, (2.8), $|\omega_{mean}|/A\Omega_0 \simeq 35$. This discrepancy might be a consequence of the lack of experimental resolution for observing the small strong vortices just formed after the roll-up of the detached boundary layers. Observation at later stages unavoidably results in lower vorticity maxima due to horizontal diffusion and is supported by

$$Re_m \approx \frac{\pi}{2}\frac{|\omega_{max}|}{A\Omega_0}\left(\frac{\rho}{L}\right)^2 Re \simeq 4500$$

(with $\rho/L \simeq 0.12$), thus substantially smaller than the prediction $Re_m \approx 9000$.

The vortices are clearly smaller in figure 5(d) than in figure 5(b). The difference in size of the vortices in these two experiments was predicted by (2.8) to scale as

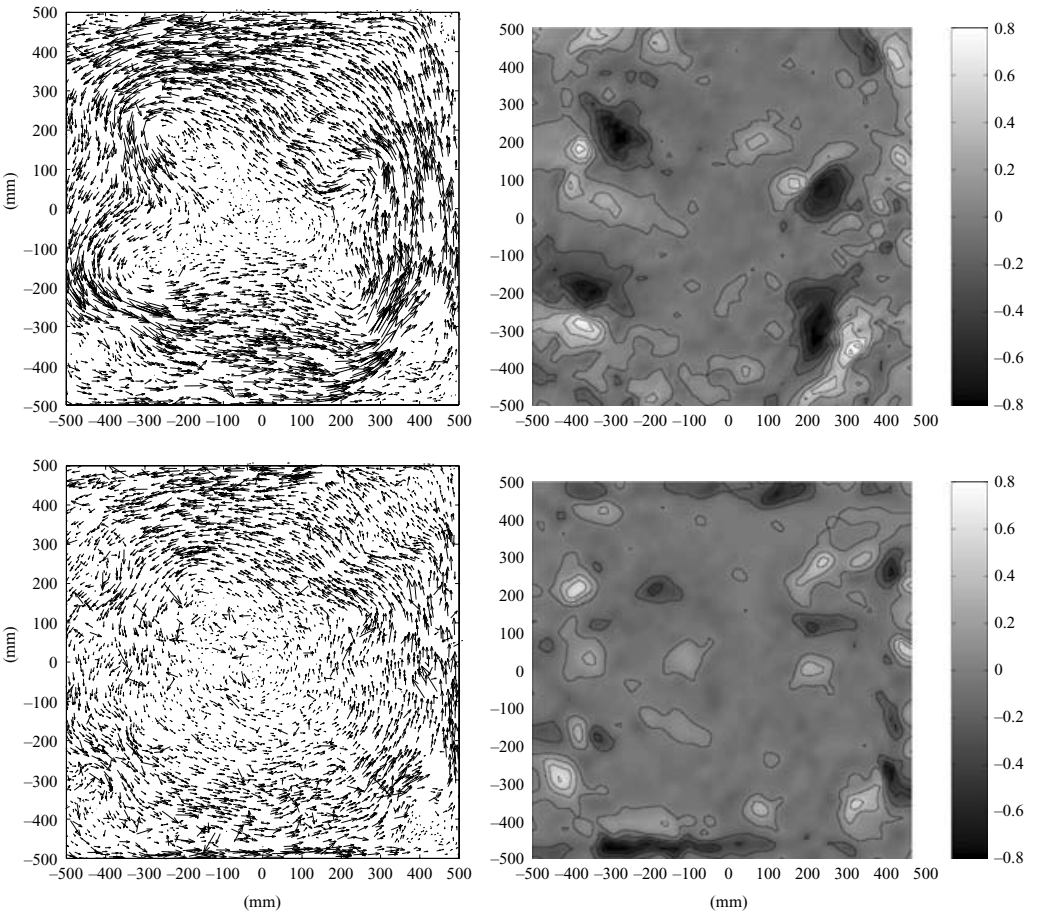

FIGURE 5. Graphs showing the flow field in the form of velocity vectors (a, c) and vorticity distributions (b, d) obtained by particle-tracking velocimetry in an experiment with $Re = 15\,000$ and $\mathscr{F} = 0.52$ (a, b) and 1.57 (c, d) (experiments 1 and 3, respectively, in table 1).

$\rho_1/\rho_3 = (f_3/f_1)^{1/4} \simeq 1.32$ (with the index denoting the experiment, see table 1), which is consistent with the observed scales in figures 5(b) and 5(d). From visual inspection, the characteristic vortex sizes were about 15 cm wide in figure 5(b) and about 12 cm in figure 5(d). The corresponding predictions for the average vortex sizes via (2.8) are 16 cm and 12 cm, respectively.

3.2. *Energy and passive scalar spectra*

Figure 6 shows the energy spectrum $E(k)$ calculated from laboratory data shown in figures 5(c) and 5(d). For this purpose, data from a two-dimensional fast Fourier transform (FFT) of the kinetic energy of the flow is collapsed onto a one-dimensional graph by computing the energy spectrum according to $E(k) = \int_k^{k+1} E(\kappa_x, \kappa_y)\,\mathrm{d}\kappa$, where $\kappa = (\kappa_x^2 + \kappa_y^2)^{1/2}$. To reduce the influence of the non-periodic boundary conditions of the velocity field, and thus the non-periodicity of the kinetic energy fields in these images, the mean (i.e. the area-averaged or total kinetic energy) is subtracted from the data and a Hanning window is applied before the Fourier transforms of the kinetic energy data were computed. The experimentally observed energy spectrum at large wavenumbers appears to decay as $E(k) \sim k^{-5/3}$. The forcing scale is assumed to be

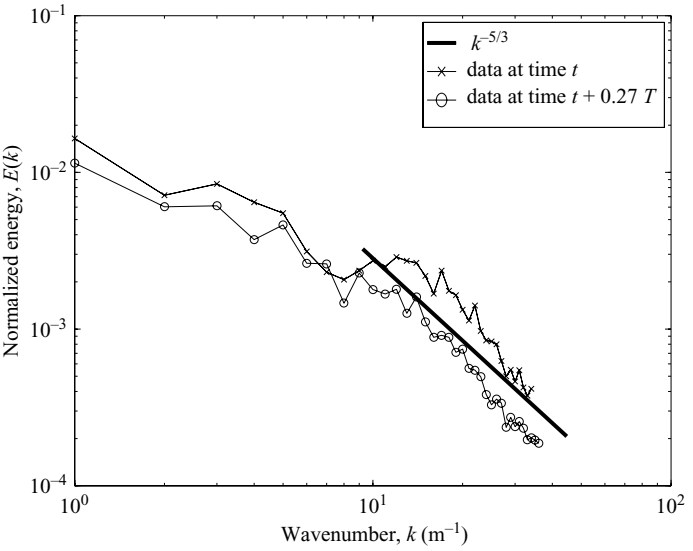

FIGURE 6. The measured energy spectrum for the laboratory experiment shown in figure 5(*c*), with $Re = 15\,000$ and $\mathscr{F} = 1.57$ (experiment 3, table 1). The spectrum has a slope similar to $k^{-5/3}$ at high wavenumbers, consistent with an inverse energy cascade. Spectra are shown for two different phases of the forcing cycle. To reduce the influence of the non-periodic boundary conditions, the mean was subtracted from the data and a Hanning window was applied before the Fourier transforms of the kinetic energy data were computed.

comparable with the thickness of the viscous boundary layer. Although for the present laboratory experiments, the flow visualization system and particle-tracking algorithm can resolve velocity scales down to 5 mm, which is slightly smaller than the predicted thickness of the Stokes boundary layer (in this case, with $Re = 15\,000$ and $\mathscr{F} = 1.57$, the layer thickness is $\delta \approx 1.5$ cm), we were unable to obtain the energy spectrum at these small scales. The smallest wavelength represented in the energy spectrum shown in figure 6 is approximately 3 cm. Numerical simulations of this experiment, which will be discussed in § 4, are conducted with a substantially higher resolution and we will be able to discuss the existence of a k^{-3} spectral slope beyond the injection scale for this kind of experiment (assuming weak or even absence of decay due to Ekman pumping).

In figure 7(*a*) a one-dimensional scalar intensity spectrum $F(k) = \int_k^{k+1} F(\kappa_x, \kappa_y)\,\mathrm{d}\kappa$ is shown, using a two-dimensional Fourier transform of the pixel intensity of images of fluorescein dye in a turbulent field. To reduce the influence of the non-periodic boundary conditions of the tracer concentration in these images, a similar procedure is used as before. The mean (i.e. the area-averaged) tracer concentration is subtracted from the data and a Hanning window is applied before the Fourier transforms are performed. An example of the images used for this spectrum is shown in figure 7(*b*) at $t/T = 1$ after the introduction of the dye. To illuminate the tank we used four slide projectors placed around the square tank, thus illuminating a 1 cm surface layer. In the following analysis, we focus on the central 512×512 pixels of the images, which represents a quarter of the total area of the tank. Pragmatic reasons force us to focus on this region in order to minimize any parallax errors in viewing the vertically aligned dye-sheets in the rotating flow. The data shown in figure 7 were taken from a sequence of images, $t/T = 0.1$ apart, in an experiment with $\mathscr{F} = 1.05$ ($A\Omega_0 = 0.06\,\mathrm{rad\,s^{-1}}$ and

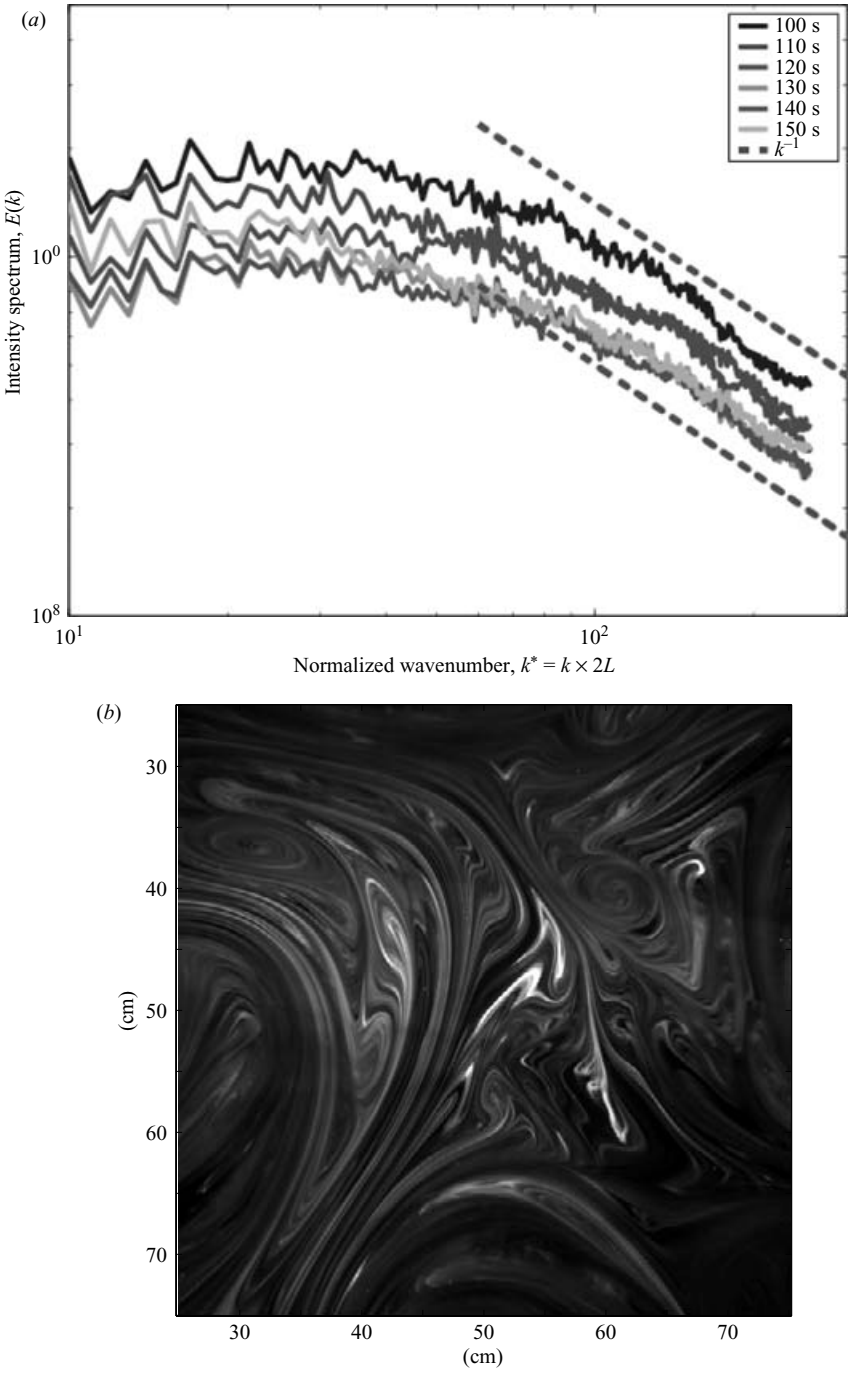

FIGURE 7. A sequence of measured intensity spectra of fluorescein dye in the turbulent flow field is plotted in (*a*) from images similar to that shown in (*b*). The spectra in (*a*) and the image in (*b*) is obtained from measurements in the central 50 cm × 50 cm of the tank in an experiment with $Re = 15\,000$ and $\mathscr{F} = 1.05$ (experiment 2, table 1). The spectra have a slope similar to k^{-1} at high wavenumbers. The mean tracer concentration was subtracted from the data and a Hanning window was applied before the Fourier transforms were performed.

$f = 0.063\,\mathrm{rad\,s^{-1}}$, a forcing period of $T = 100\,\mathrm{s}$). Although $\mathscr{F}$ is slightly different for both experiments discussed here (and the Reynolds number the same), the average boundary-layer thickness and the wavenumber for the anticipated change from a $k^{-5/3}$-range to a k^{-3}-range, is approximately the same for both experiments. After the experiment had run for 10 min, 5 ml of fluorescein dye was injected into the surface layer of water in one corner of the tank. The striking feature of figure 7(a) is the k^{-1} power-law behaviour of the spectra, consistent with the predictions of Batchelor (1959). Apparently, the overall intensity of the dye, initially introduced in the surface layer, shows a gradual decrease. This is attributed to the recirculating flow induced by Ekman pumping. This results in average upward transport of undyed fluid in the vortex cores and an accompanying average downward transport of dyed fluid to the bottom. Once dye is removed from the surface layer it will not be detected.

Theoretically, a k^{-1} power law of the scalar spectrum should occur in the same spectral range as the enstrophy cascade of the energy spectrum. It was impossible to resolve a high-wavenumber enstrophy cascade from the velocity measurements, but we note that the k^{-1} power law occurs at wavenumbers $k \gtrsim 80\,\mathrm{m^{-1}}$, which is in the region where such an enstrophy cascade is indeed expected.

4. Direct numerical simulations of oscillating spin-up

In a co-rotating frame of reference, the effect of a time-dependent uniform background rotation, is described by a forcing term $\boldsymbol{k}\cdot\nabla\times(\mathrm{d}\boldsymbol{\Omega}/\mathrm{d}t\times\boldsymbol{r}) = 2\,\mathrm{d}\Omega(t)/\mathrm{d}t$, with $\boldsymbol{k} = \boldsymbol{\Omega}/|\boldsymbol{\Omega}|$ the unit vector in the axial or z-direction, in the vorticity equation:

$$\frac{\partial\omega}{\partial t} + (\boldsymbol{v}\cdot\nabla)\omega = \nu\nabla^2\omega - 2A\Omega_0 f\cos(ft), \tag{4.1}$$

where the relation $\Omega(t) = \Omega_0(1 + A\sin(ft))$ is used, $\boldsymbol{v} = (u, v)$ and $\omega = \partial v/\partial x - \partial u/\partial y$ is the axial component of the vorticity (with x and y the Cartesian coordinates).

The numerical simulations are performed with a Chebyshev pseudospectral code developed by Clercx (1997). The computational domain $\mathscr{D}$ is the square $[-1, 1]\times[-1, 1]$ with boundary $\partial\mathscr{D}$. On this domain, the vorticity equation in the co-rotating frame of reference can be written in the dimensionless form

$$\frac{\partial\omega}{\partial t} + (\boldsymbol{v}\cdot\nabla)\omega = \frac{1}{Re}\nabla^2\omega - 2\mathscr{F}\cos(\mathscr{F}t), \tag{4.2}$$

where time has been made dimensionless with $A\Omega_0$. The Reynolds number is defined as in (2.3). The vorticity equation (4.2) must be solved in combination with the relations

$$\nabla^2\boldsymbol{v} = \hat{\boldsymbol{e}}_z\times\nabla\omega \quad \text{on } \mathscr{D}, \tag{4.3}$$

$$\hat{\boldsymbol{e}}_z\cdot\nabla\times\boldsymbol{v} = \omega \quad \text{on } \partial\mathscr{D}, \tag{4.4}$$

$$\boldsymbol{v} = 0 \quad \text{on } \partial\mathscr{D}. \tag{4.5}$$

The time discretization of the vorticity equation consists of a second-order explicit Adams–Bashforth scheme for the advection term and an implicit Crank–Nicolson procedure for the diffusion term.

In figure 8, the vorticity field is plotted for $\mathscr{F} = 1.25$. The Reynolds number is $Re = 20\,000$ in figure 8(a) and $Re = 5000$ in figure 8(b). Full details of all numerical parameters are given in tables 2 and 3; the results from runs 44 and 29 are shown in figure 8. The fields are seeded with the initial noise required to remove the fourfold rotation symmetry present owing to the forcing protocol. This was done

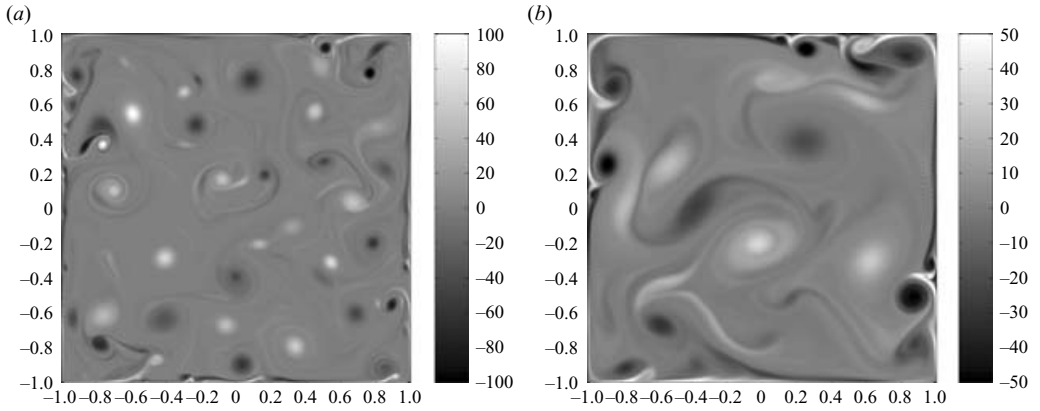

FIGURE 8. Vorticity distributions obtained by numerical simulations representing the flow at $t = 50$ (after approximately 10 forcing periods), showing the turbulent vorticity field for (*a*) $Re = 20\,000$ and (*b*) $Re = 5000$ for $\mathscr{F} = 1.25$. Note the smaller vortex size at larger Re. In both figures many filaments, detached from the boundaries or from strained vortices, can be observed, and no large-scale (i.e. domain-filling) vortex structures are absent. These two simulations are runs 44 and 29, respectively, in table 3.

Re	N	Δt
500	120	5.0×10^{-4}
1000	160	2.5×10^{-4}
2000	160	2.5×10^{-4}
5000	200	2.0×10^{-4}
10 000	288	1.0×10^{-4}
15 000	324	8.0×10^{-5}
20 000	400	5.0×10^{-5}

TABLE 2. A summary of all numerical parameters used in the simulations discussed in the paper. N denotes the order of Chebyshev polynomials used in the expansion (corresponding to a resolution $(N+1)^2$) and Δt denotes the time step of the simulation. All simulations have run 50 dimensionless time units, i.e. approximately $8\mathscr{F}$ forcing periods.

by applying random noise of amplitude 0.01 to the initial vorticity field in the first 10×10 Chebyshev modes. The predicted thickness of the boundary layer by (2.5) for $Re = 20\,000$ (figure 8*a*) is half that of $Re = 5000$ (figure 8*b*). In both cases, there are regions near the boundaries where new vortices are formed by the separation and roll-up of the boundary layer. The difference in size of the emerging vortices is then directly related to the difference in boundary-layer thickness – hence the larger vortices are seen in the simulation with $Re = 5000$. As the maximum vorticity for fixed $\mathscr{F}$ scales with the square root of the Reynolds number by (2.7), the averaged maximum vorticity values of the vortices near the boundaries in figure 8(*a*) are expected to be approximately twice those observed in figure 8(*b*). This is indeed observed, $|\omega_{max}|/A\Omega_0 \approx 50$ and 25, respectively.

An interesting aspect of these numerical experiments is the presence of strong filaments of vorticity, which we were unable to resolve in the laboratory measurements. Some of these filaments in figure 8 are in the process of roll-up to form new vortices, others are due to vortices interacting with the wall and creating new filaments from the

Run	Re	$\mathscr{F}$	$\lvert\omega_{mean}\rvert$	ρ_{mean}/L	Run	Re	$\mathscr{F}$	$\lvert\omega_{mean}\rvert$	ρ_{mean}/L
1	500	0.05	1.61	0.403	23	5000	0.05	3.11	0.329
2		0.10	3.10	0.390	24		0.10	6.65	0.290
3		0.20	4.61	0.338	25		0.20	7.95	0.248
4		0.50	5.17	0.311	26		0.50	9.75	0.211
5		0.80	5.23	0.295	27		0.80	14.4	0.189
6		1.00	5.98	0.288	28		1.00	16.0	0.173
7		1.25	6.86	0.295	29		1.25	17.5	0.160
8		1.50	6.72	0.307	30		1.50	15.3	0.159
9		1.75	6.50	0.317	31		1.75	15.0	0.163
10	1000	0.05	1.66	0.399	32	10000	0.20	11.6	0.207
11		0.10	4.64	0.352	33		0.50	20.5	0.184
12		0.20	4.59	0.312	34		0.80	23.1	0.158
13		0.50	6.44	0.285	35		1.00	23.0	0.148
14		0.80	7.09	0.263	36		1.25	22.9	0.143
15		1.00	8.34	0.241	37		1.50	22.7	0.130
16		1.25	9.92	0.249	38		1.75	20.0	0.137
17		1.50	8.66	0.267	39	15000	0.80	21.3	0.145
18		1.75	8.75	0.301	40		1.00	25.4	0.130
19	2000	0.50	7.75	0.253	41	20000	0.50	27.1	0.143
20		0.80	9.56	0.225	42		0.80	32.3	0.127
21		1.00	10.0	0.214	43		1.00	30.2	0.116
22		1.25	11.1	0.200	44		1.25	26.6	0.121
					45		1.50	27.0	0.116

TABLE 3. A summary of the parameters used in the simulations discussed in the paper (with the dimensionless Ekman decay rate $\mathscr{A} = 0$). $\mathscr{F}$ represents the dimensionless forcing frequency. The last two columns represent the dimensionless mean vortex amplitude, $|\omega_{mean}|$, and the average vortex radius, ρ_{mean}/L, respectively.

wall, and some are due to vortex–vortex interactions where vorticity can be stripped off the perimeter of a weaker vortex by a strong vortex. These weak filaments of vorticity are eventually destroyed by viscous dissipation.

4.1. *The threshold for dipole formation*

In § 2, we introduced a condition for dipole formation: $\mathscr{F} < 2$. We also briefly discussed experimental evidence that dipole formation actually occurs for $\mathscr{F} \lesssim 1.7$. Both the presence and the approximate value of the threshold for dipole formation is confirmed by the numerical simulations (for the values of Re and $\mathscr{F}$, see table 3). From these simulations we determined the (dimensionless) enstrophy of the interior of the domain,

$$V_{int}(t) = \tfrac{1}{2} \int_{-0.75}^{0.75} \int_{-0.75}^{0.75} \omega^2(x, y, t)\, \mathrm{d}x\, \mathrm{d}y.$$

The boundary layers, biasing the enstrophy by the large-amplitude vorticity present near the no-slip walls, are automatically excluded in determining $V_{int}(t)$. The sudden increase of $V_{int}(t)$ in the course of time is associated with the emergence of vortex structures in the centre of the container, thus indirectly indicating dipole formation. The interior enstrophy is computed for each dimensionless time unit. Note that the sinusoidal forcing is reflected in the oscillations of $V_{int}(t)$.

We have plotted $V_{int}(t)$ for $\mathscr{F} = 0.2$, 0.5 and 1.0 (figure 9*a*) and for $\mathscr{F} = 1.0$, 1.5 and 2.0 (figure 9*b*) obtained from runs with $Re = 5000$. Similar results are available

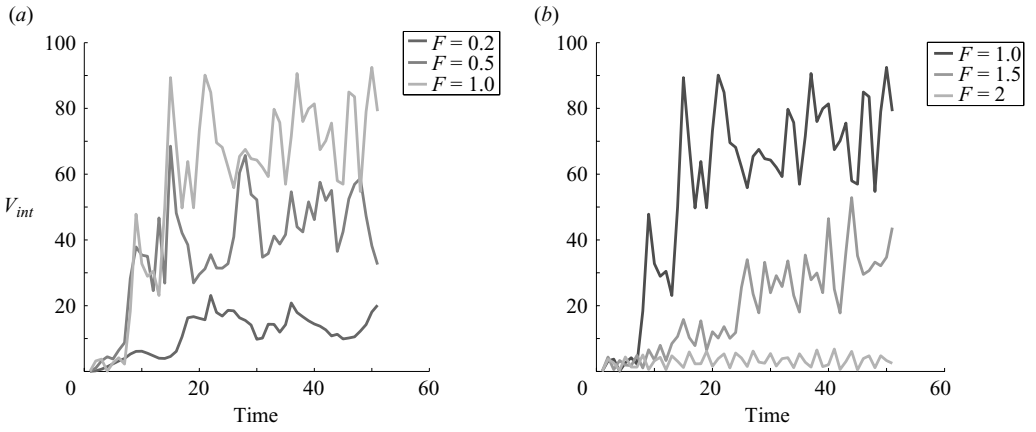

FIGURE 9. Time evolution of $V_{int}(t)$ for numerical simulations with $Re = 5000$. (*a*) data for $\mathscr{F} = 0.2$, $\mathscr{F} = 0.5$ and $\mathscr{F} = 1.0$, (*b*) data for $\mathscr{F} = 2.0$, $\mathscr{F} = 1.5$, and (for reference) $\mathscr{F} = 1.0$.

for the runs with different Reynolds number (provided $Re \geqslant 2000$), but they are not shown here. In particular, for $\mathscr{F} = 0.5$ and 1.0, we observe a sudden increase of V_{int} after approximately two forcing periods. For $\mathscr{F} = 1.5$, a substantial increase of V_{int} can still be seen, but dipole formation seems to be delayed and the resulting dipoles are weaker; for $\mathscr{F} = 2.0$, no increase of V_{int} is observed beyond the weak oscillatory variation in time. Finally, the low-frequency case ($\mathscr{F} = 0.2$) does not indicate clear dipole formation yet. Apparently, the total number of forcing periods (less than two) was too small to observe appreciable dipole formation.

Finally, figure 10 shows the time-averaged value of $\overline{V}_{int}$ for three different Reynolds numbers (2000, 5000 and 10 000) and $\mathscr{F} \leqslant 2.0$. From these data, we can conclude that $\overline{V}_{int}$ strongly decreases for $\mathscr{F} \gtrsim 1.0$. Moreover, combining the scaling relations from (2.8) indicates that $\overline{V}_{int} \propto Re\mathscr{F}$, a trend clearly visible in figure 10 with the initial linear increase in $\overline{V}_{int}$ for $\mathscr{F} \leqslant 1$, and with the magnitude of $\overline{V}_{int}$ increasing with Re. Note again that for small $\mathscr{F}$, the number of forcing periods in the numerical simulations is presumably too small, which also leads to the reduced values for $\overline{V}_{int}$.

We can conclude here that the numerical data shown in figures 9 and 10, together with a few available experimental observations, clearly support our estimate of the threshold of dipole formation put forward in § 2.

4.2. *The average vortex size*

A measure of the average vortex size in the turbulent flow is required to test the scaling relation $\rho_{mean}/L \propto (Re\mathscr{F})^{-1/4}$. The mean-square wavenumber of the vortices can be estimated straightforwardly by the ratio of enstrophy $V = \frac{1}{2}\int_{\mathscr{D}} \omega^2 \, \mathrm{d}A$ and energy $E = \frac{1}{2}\int_{\mathscr{D}} \boldsymbol{u}^2 \, \mathrm{d}A$, and yields $\langle k^2 \rangle \sim V/E$. The average radius of the vortices is then $\rho_{mean} \sim \frac{1}{2}\lambda \sim \pi L\sqrt{E/V}$, with $\lambda = (2\pi/k)L$ the mean wave length in the flow. Strictly speaking, the estimates for $\langle k^2 \rangle$ and λ are valid for homogeneous and isotropic turbulence, which is not the case in the present numerical experiments. Nevertheless, we assume that it is legitimate to apply these estimates for $\langle k^2 \rangle$ and λ to obtain estimates for ρ_{mean}.

The highest enstrophy values are found in the boundary layers. The presence of boundary layers implies the existence of a characteristic wavenumber k_δ which scales with $\sqrt{Re}$. If the size of the eddies in the interior has to be estimated, a thin boundary region of thickness $\epsilon \gtrsim 1/k_\delta$ is excluded from the calculation of the enstrophy. If this

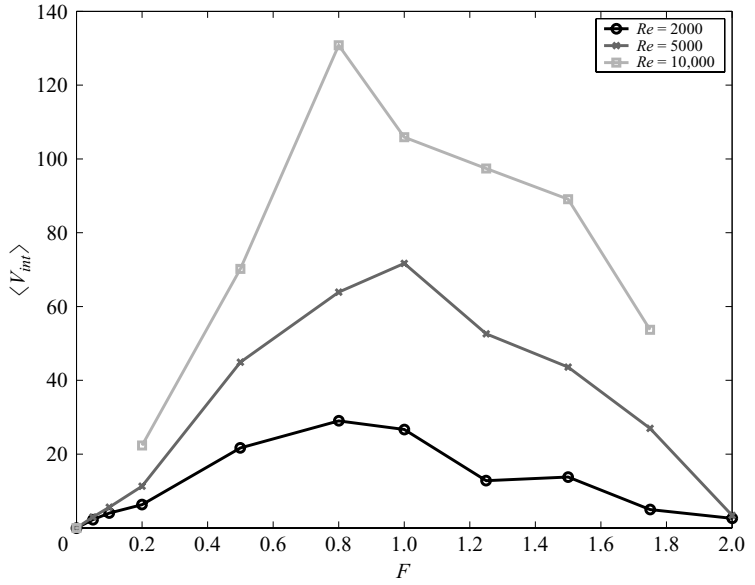

FIGURE 10. The average interior enstrophy $\overline{V}_{int}$ is plotted as function of $\mathscr{F}$ with $\mathscr{F} \leqslant 2.0$. Three different Reynolds numbers are considered: $Re = 2000$, $Re = 5000$ and $Re = 10\,000$. Based on the scaling arguments of (2.8), we expect that $\overline{V}_{int}$ will increase linearly with both Re and $\mathscr{F}$, as observed for $\mathscr{F} < 1$. For $1 < \mathscr{F} < 2$, $\overline{V}_{int}$ decreases as dipoles become more difficult to form, until $\overline{V}_{int} = 0$ at $\mathscr{F} = 2$, as predicted by (2.2).

correction is not used, the wavenumber estimated by $k \approx \sqrt{V/E}$ then predominantly represents the smaller thickness of the boundary layer, rather than the average size of the vortices, owing to the extremely high vorticity values in the boundary layers. This can easily be shown by the following estimate. The vorticity in the interior, ω_i, is proportional to the forcing, $\omega_i \approx 2A\Omega_0$, which yields for the associated enstrophy: $V_i \approx 8(A\Omega_0 L)^2$. The vorticity in the boundary layers is estimated to be $\omega_{max} \approx A\Omega_0 L/\delta$, and the enstrophy in the boundary layer is $V_\delta \approx 4L\delta\omega_\delta^2$. It can be concluded that $V_\delta / V_i \approx L/(2\delta) \propto \sqrt{Re}$, and V_δ will largely dominate the total enstrophy and thus also the computed value of $\langle k^2 \rangle$ if no correction is taken into account.

The observed size of vortices formed for various Re and $\mathscr{F}$ is plotted against the theoretical prediction $\rho_{mean}/L \propto (Re\mathscr{F})^{-1/4}$ in figure 11, yielding the constant of proportionality used in (2.8). The data used in this figure are from the runs summarized in table 3. When the vortices are small, there is good agreement with the theoretical prediction. Deviations are observed for the low-Reynolds-number runs only, i.e. $Re = 500$ and 1000; in these cases, the new vortices occupy nearly a quarter of the tank each and the scaling argument leading to predictions of the vortex size and amplitude as function of Re and $\mathscr{F}$ might be invalidated. On average, the vortex sizes computed according to our definition are slightly less than the predicted value.

The observation that the maximum size of the eddies scales with their initial size implies that there are very few interactions between vortices that lead to merger and the formation of larger-scale vortices, and that on average the ageing vortices are actually destroyed by the younger ones. The mergers that are observed in the numerical simulations happen in conjunction with a considerable amount of filamentation induced by neighbouring vortices and by the background shear. No substantial increase in size is observed after a (partial) merger.

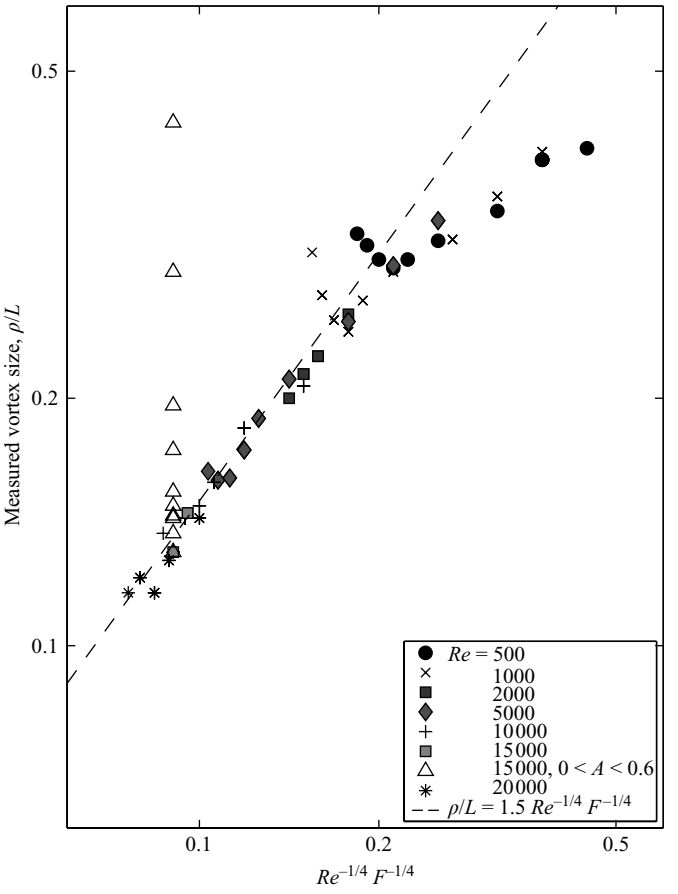

FIGURE 11. Plot of the vortex size for varying Re and $\mathscr{F}$. Shown are results from numerical experiments using $\rho/L \sim \pi\sqrt{E/V}$. The parameters used for the simulations are summarized in table 3. For either high Re and larger $\mathscr{F}$, small vortices form, and their size appears to be in good agreement with theory (straight dashed line). When larger vortices form (low Re or the smaller values of $\mathscr{F}$) the observations diverge from the scaling relation (2.8). This is a finite-size effect allowing a minimum of four vortices in the tank. The maximum vortex sizes observed in the numerical simulations, as well as in the experiments shown in figures 3 to 5, were always $\rho/L < 0.5$.

4.3. *The decay of vortices*

Vortices decrease in size when filaments of vorticity are stripped off during strong shearing events (Mariotti, Legras & Dritschel 1994; Dritschel & Zabusky 1996; Trieling, Beckers & van Heijst 1997). Many such filaments can be seen in figure 8, where weaker vortices formed on previous cycles (older vortices) are being destroyed by the new set of vortices. To illustrate how individual vortices decrease in size and strength with time in the numerical simulation, several vortices were tracked after they formed in the corners of the tank and the change in their size and circulation was recorded as a function of time. There is some difficulty in distinguishing between the high-vorticity regions of the rotationally dominated vortex cores and the filaments of vorticity being stripped off by background shear. One way to identify the vortex cores is to distinguish between regions that are locally dominated by rotation (the vortex core) and regions that are dominated by strain. For this purpose, we can use the

criterion proposed by Okubo (1970) and Weiss (1991). Regions of the flow dominated by either rotation or strain can be distinguished by the sign of the quantity,

$$Q = S^2 - \omega^2, \tag{4.6}$$

where S is a measure of the local strain and defined as $S = -\det(\nabla \boldsymbol{v} + \nabla \boldsymbol{v}^T)$. The regions of the vortex cores, which are dominated by rotation, have $Q < 0$, while the surrounding strain dominated regions have $Q > 0$. In flows with strong vortex filaments, a stronger criterion is required. The method we have used to identify vortices is illustrated in figure 12, where results are plotted from a numerical simulation with $Re = 15\,000$ and $\mathscr{F} = 1.00$ (run 40 in table 3). Figures 12(a) and 12(b) show the vorticity field and the Okubo–Weiss function Q, respectively. Figure 12(c) shows the vorticity field, which is overlain by contours identifying the coherent structures. These contours bound the regions where $Q < -150$ and $|\omega| > 5$. A geometric criterion was also used to elimate strong vortex filaments by requiring that the vortices must be approximately circular. This was achieved by comparing the second moment of the distribution of vorticity inside a contour to the second moment of a uniform circular distribution of the same pixel area; if this ratio is greater than 2, then the structure is too long and filamental, and is hence rejected.

The trajectories of approximately 50 vortex centres observed in the run with $Re = 15\,000$ and $\mathscr{F} = 1.00$ (followed for a period of 1.5 forcing cycles) are shown in figure 13(a). The average value of the vorticity within the vortices is plotted in figure 13(b) as a function of time, and we can see that on average the vortex amplitude decreases with time. Nevertheless, a well-defined mean value can be extracted, $|\omega_{mean}| \approx 25$. The average initial radius of these vortices is around $(0.12 \pm 0.04)L$ (consistent with data in table 2, run 40). The absolute value of the ratio of maximum initial circulation of these vortices, to the maximum circulation due to the forcing is approximately one-eighth, as predicted and $Re_m \approx 0.57Re$, close to the predicted $Re_m \approx 0.6Re$. This is consistent with the ideas put forward in § 2.1 that every period, eight new vortices are formed such that their total circulation is equal and opposite to the circulation induced by the forcing.

Figure 14 presents values of the average vorticity within coherent vortex structures for the numerical experiments 1–45 (table 3) and the results are compared with the theoretical prediction $|\omega_{mean}|/A\Omega_0 \propto \sqrt{Re\mathscr{F}}$. The magnitude of the average vorticity in the vortex structures is calculated by identifying the vortex structures in each run in the same manner as shown in figure 12(c). As noted in figure 13(b), there is a well-defined mean to the vorticity in these flows, and figure 14 shows a good agreement of the measured values of $|\omega_{mean}|$ with the predicted scaling.

For comparison, the two experimental observations, taken from figures 5(b) and 5(d), are plotted as well. The measured value of $|\omega_{mean}|$ from these experiments shows good agreement with the numerical simulations (keeping corrections in mind owing to Ekman decay).

4.4. *The effects of Ekman damping*

The effect of Ekman pumping in numerical simulations of two-dimensional flows can be modelled by including a linear damping term in the two-dimensional vorticity equation (4.2) (see Pedlosky 1987) to give,

$$\frac{\partial \omega}{\partial t} + (\boldsymbol{v} \cdot \nabla)\omega = \frac{1}{Re}\nabla^2 \omega - 2\mathscr{F}\cos(\mathscr{F}t) - \mathscr{A}\omega. \tag{4.7}$$

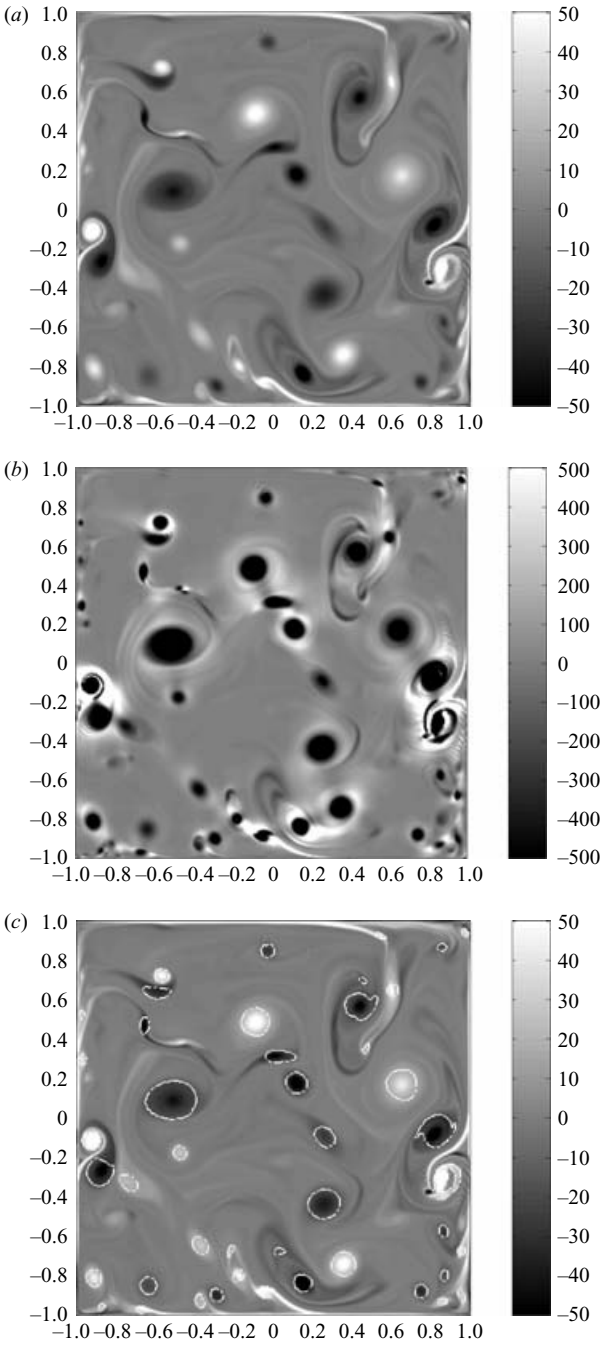

FIGURE 12. (*a*) The distribution of the vorticity ω, and (*b*) the Okubo–Weiss function Q, which is used as a criterion for determining the size of the vortex cores. In (*c*) contours defining the extent of the coherent structures (with $Q < -150$ and $|\omega| > 5$) are overlain on the vorticity distribution. This numerical simulation was carried out for $Re = 15\,000$ and $\mathscr{F} = 1.00$ (run 40, table 3). An animation of the vorticity in this numerical simulation is available as a supplement to the online version of the paper.

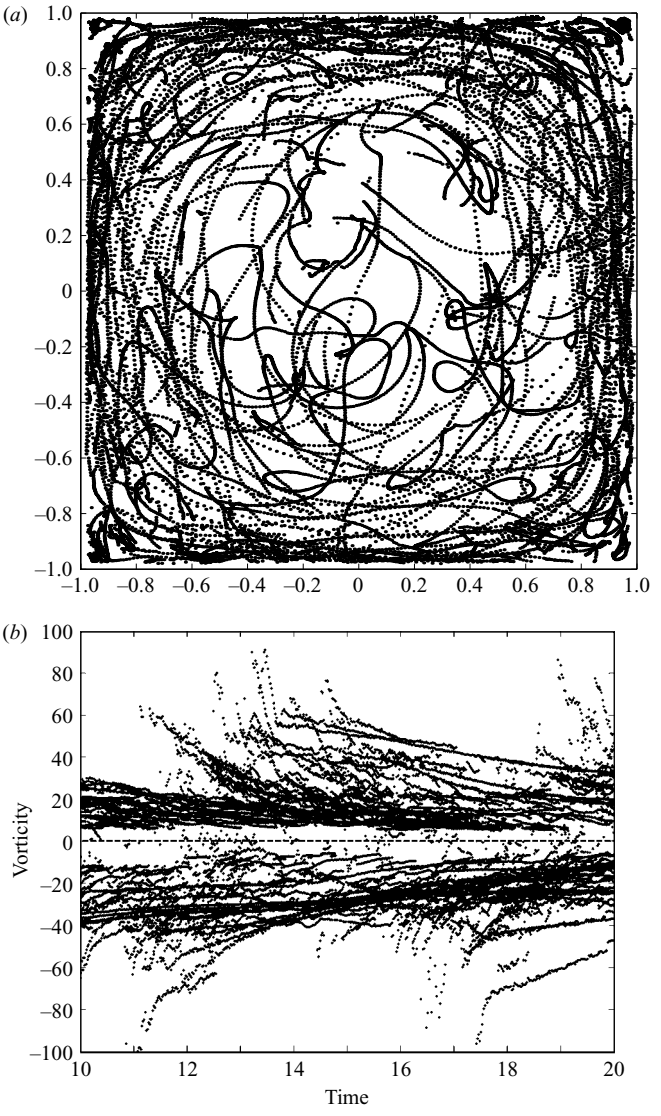

FIGURE 13. The trajectories of approximately 50 vortices of the numerical simulation shown in figure 12 are plotted in (*a*) over a period of 1.5 forcing cycles. The vortex amplitudes as a function of time are plotted in (*b*). The mean values of the vorticity within a vortex can be seen to start quite high ($\omega = \pm 50$–60) before rapidly decaying to values in the range $\omega = \pm 20$–30. Ekman damping is absent in this run, so this decay of the mean vorticity is due to lateral diffusion and vortex stripping only.

Here, the linear Ekman pumping decay rate $\alpha = 1/T_E$ is non-dimensionalized using $\mathscr{A} = \alpha L/U = \alpha/(A\Omega_0)$ and $\mathscr{F} = f/(A\Omega_0)$ (note for comparison with the experiment: $\mathscr{A}/\mathscr{F} = \alpha/f$). It was observed that even without a linear damping term, the kinetic energy of the two-dimensional turbulent flow reaches a statistically steady value, owing to the no-slip boundary conditions. Inclusion of the linear damping term will lead to more rapid destruction of vortex filaments generated at the boundary and will result in lower mean energies and lower peak vorticity in the vortex cores. In laboratory experiments, the effect of Ekman pumping may be important for

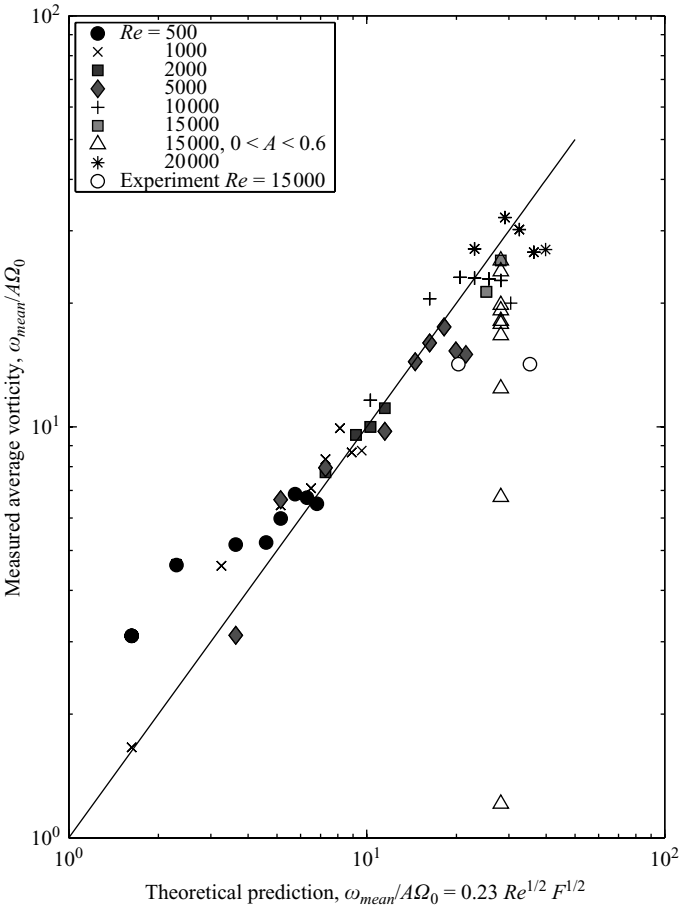

FIGURE 14. A comparison of the mean vortex amplitude obtained from the numerical simulations (table 3) and the laboratory experiments 1 and 3 from table 1 with the theoretical prediction that $|\omega_{mean}| \propto \sqrt{Re\mathscr{F}}$. The mean vorticity is computed with the procedure explained in figures 12 and 13. The data show good agreement with the theoretical prediction. Data from laboratory experiments are taken from figure 5. The laboratory experiments are affected by Ekman damping (in particular experiment 3) so have lower values of mean vorticity than those from numerical simulations where Ekman damping is absent.

the vortex dynamics, so this process has been explored using a series of numerical experiments in which the decay rate $\mathscr{A}$ is increased relative to the forcing frequency $\mathscr{F}$. These simulations were carried out for $Re = 15\,000$ and $\mathscr{F} = 1.00$, a regime comparable to the laboratory experiments 1–3 of table 1 (with $\mathscr{F} = 0.52$, 1.05 and 1.57, respectively). The following range of dimensionless Ekman decay rates have been used: $\mathscr{A} = 0.00$, 0.02, 0.04, 0.06, 0.08, 0.10, 0.15, 0.20, 0.40 and 0.60 (see table 2 for details of the numerical parameters). The resulting vorticity distribution at $t/T = 50$ is shown in figure 15 for six different cases in which the ratio $\mathscr{A}/\mathscr{F}$ is varied from 0 to 0.60. The first case with no damping ($\mathscr{A}/\mathscr{F} = 0$, figure 15*a*) shows strong vortex interactions and the presence of vorticity filaments. The maximum absolute values of vorticity are about 40 and the flow is highly disordered. As the damping is slowly increased from $\mathscr{A}/\mathscr{F} = 0.02$, through $\mathscr{A}/\mathscr{F} = 0.06$, to $\mathscr{A}/\mathscr{F} = 0.10$ (figure 15*b–d*), vortices are still seen to form and the flow appears turbulent, but the maximum

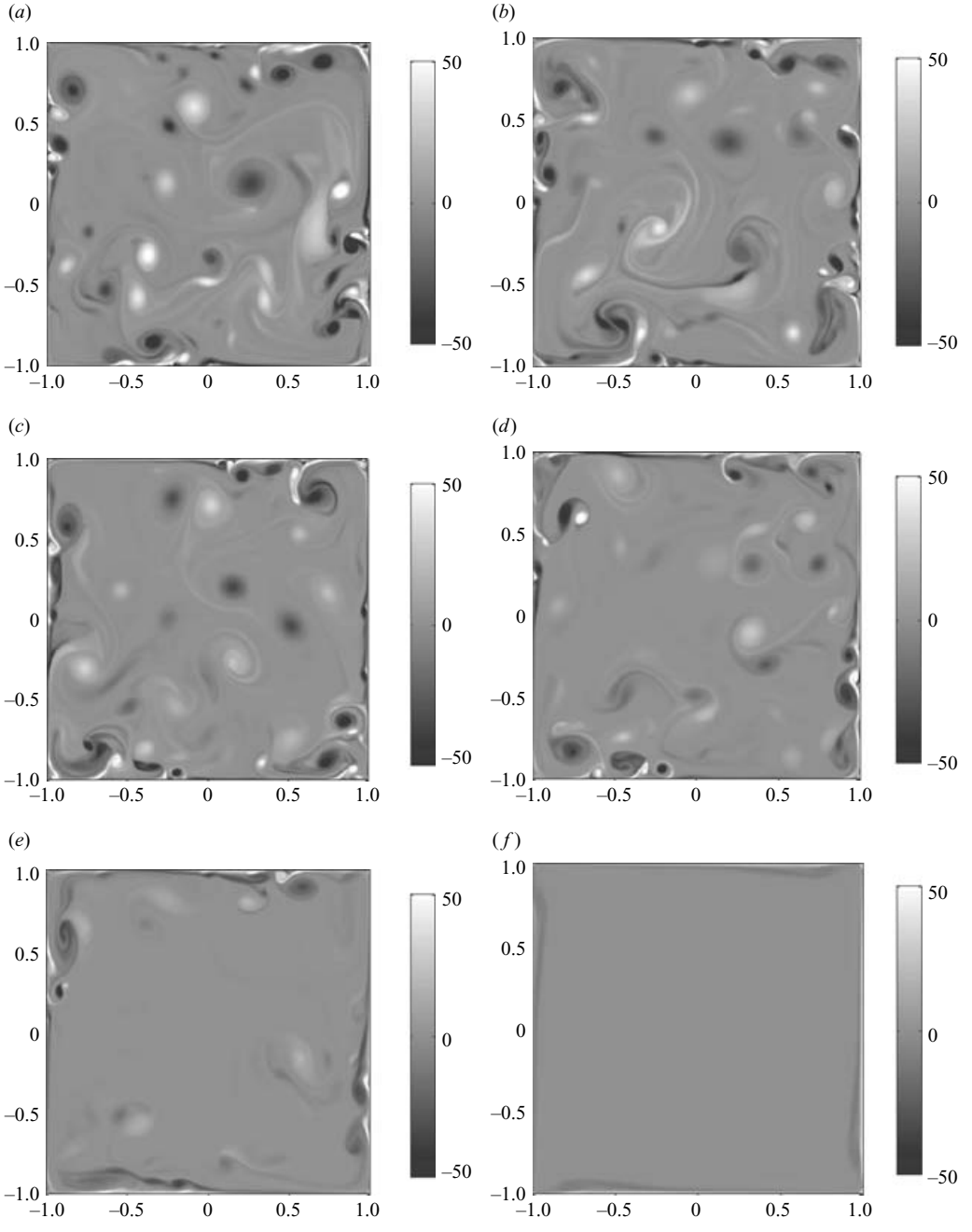

FIGURE 15. Vorticity distributions for different values of $\mathscr{A}/\mathscr{F}$ with $Re = 15\,000$ and $\mathscr{F} = 1.00$ at $t/T = 50$. The values of $\mathscr{A}/\mathscr{F}$ used in the displayed vorticity fields of the simulations are (*a*) 0, (*b*) 0.02, (*c*) 0.06, (*d*) 0.10, (*e*) 0.20 and (*f*) 0.60. Simulations with $\mathscr{A}/\mathscr{F} = 0.06$ and 0.10 are comparable to the experiments shown in figure 5. Details of the numerical parameters can be found in tables 2 and 4.

vorticity values (in particular the older vortices that have moved to the interior of the flow domain) and the number of vorticity filaments decrease. When $\mathscr{A}/\mathscr{F} = 0.20$, see figure 15(*e*), the damping causes a substantial decrease in the strength of vortices

from one period to the next, such that vortex–vortex stripping interactions are no longer the principal determinant of the vortex size, and the Ekman decay is becoming dominant. As the vortex interactions are suppressed, we also note that the symmetry of the underlying forcing can be seen in the resulting vorticity distributions. When $\mathscr{A}/\mathscr{F} = 0.60$, the damping is so strong that the vortices cannot form and the only strong vorticity present is near the no-slip boundaries (see figure 15*f*).

In figures 11 and 14 we have plotted the vortex size and amplitude (the triangles in these figures), respectively, obtained from these numerical simulations (with fixed Re and $\mathscr{F}$) for varying dimensionless Ekman decay rate $\mathscr{A}$. From these data we can conclude that for $Re = 15\,000$ and $\mathscr{F} = 1.00$ the data with $\mathscr{A} \lesssim 0.15$ are very similar to those from the runs without Ekman decay. From this comparison, we may conclude that the effects of the Ekman decay rate on ρ_{mean} and ω_{mean} in the experiments are small.

The reduction of dipole formation as a result of Ekman damping is also illustrated well by plots of $V_{int}(t)$ and $\overline{V}_{int}$ for several values of $\mathscr{A}/\mathscr{F}$. In figure 16(*a*), we have shown $V_{int}(t)$ for $\mathscr{A}/\mathscr{F} = 0.00$, 0.02, 0.04 and 0.08. In figure 16(*b*), we have displayed similar data, but now for $\mathscr{A}/\mathscr{F} = 0$ (for reference), 0.10, 0.20 and 0.40. Finally, figure 16(*c*) shows the decrease of $\overline{V}_{int}$ with increasing $\mathscr{A}$. The decay is exponential for $\mathscr{A}/\mathscr{F} \lesssim 0.20$.

For comparison, the laboratory experiments illustrated by the images shown in figures 3 to 5 had a forcing frequency of $f = 0.031$–$0.126\,\mathrm{rad\,s^{-1}}$ ($T = 200$ to 50 s) and an Ekman decay period of 200 s using $T_E = H/\sqrt{\nu\Omega_0}$ with $H = 20\,\mathrm{cm}$, $\nu = 1 \times 10^{-2}\,\mathrm{cm^2\,s^{-1}}$ and $\Omega_0 = 1\,\mathrm{rad\,s^{-1}}$ so that $0.04 < \mathscr{A}/\mathscr{F} < 0.16$ (note that by definition $\mathscr{A}/\mathscr{F} = \alpha/f$). This small ratio indicates, keeping in mind the results of our numerical simulations with Ekman damping (figure 15), that linear Ekman decay is not the most important process in the laboratory experiments. The vorticity plots shown in figures 5(*a*) and (*b*) had $\mathscr{A}/\mathscr{F} = 0.053$ and in figures 5(*c*) and 5(*d*) $\mathscr{A}/\mathscr{F} = 0.161$, so they are comparable to the simulations shown in figures 15(*c*) and 15(*d*). There is also good agreement between the numerically obtained vorticity maxima and the observed values in the laboratory experiments. For laboratory experiments 1 and 3, dimensionless vorticities of $|\omega_{mean}|/A\Omega_0 \approx 13$–14 were observed, which are comparable with the numerical values of $|\omega_{mean}|/A\Omega_0 \approx 12$–19, as given in table 4 for the runs with $Re = 15\,000$, $\mathscr{F} = 1.00$ and different values of the dimensionless bottom friction $\mathscr{A}$.

4.5. *Energy spectra from numerical simulations*

Figure 17 shows phase-averaged kinetic energy spectra (based on Chebyshev expansion coefficients), obtained by numerical simulations of forced turbulence for Reynolds numbers $Re_1 = 5000$, $Re_2 = 10\,000$, $Re_3 = 15\,000$, and $Re_4 = 20\,000$, respectively, and $\mathscr{F} = 0.80$ (for all four runs). Note that a k^{-n} Fourier spectrum results in the same power-law Chebyshev spectrum; a direct comparison of Fourier spectra and Chebyshev spectra is thus allowed. These are the runs 27, 34, 39 and 42, respectively, in table 3 (for the resolution of these runs, see table 2). The non-dimensional boundary-layer thickness scales as $\sqrt{Re}$ (it should be noted that $\mathscr{F} = 0.80$ in these runs), so it is expected that the ratio of the boundary-layer thicknesses from the four simulations should scale as $\sqrt{Re_4/Re_1} = 2.0$, $\sqrt{Re_3/Re_1} = 1.7$ and $\sqrt{Re_2/Re_1} = 1.4$. The displayed spectra in figure 17 clearly indicate that the 'knee' where the slope changes from $k^{-5/3}$-like to k^{-3}-like behaviour lies at approximately $k = 90$ (Re_1), 130 (Re_2), 170 (Re_3), and 200 (Re_4), i.e. at ratios similar to those predicted.

The phase-averaged energy spectra from the numerical simulations with Ekman damping are plotted in figure 18(*a*). The laboratory experiments were in the range $0.04 < \alpha/f < 0.16$, and the numerical simulations indicate that for this range both a

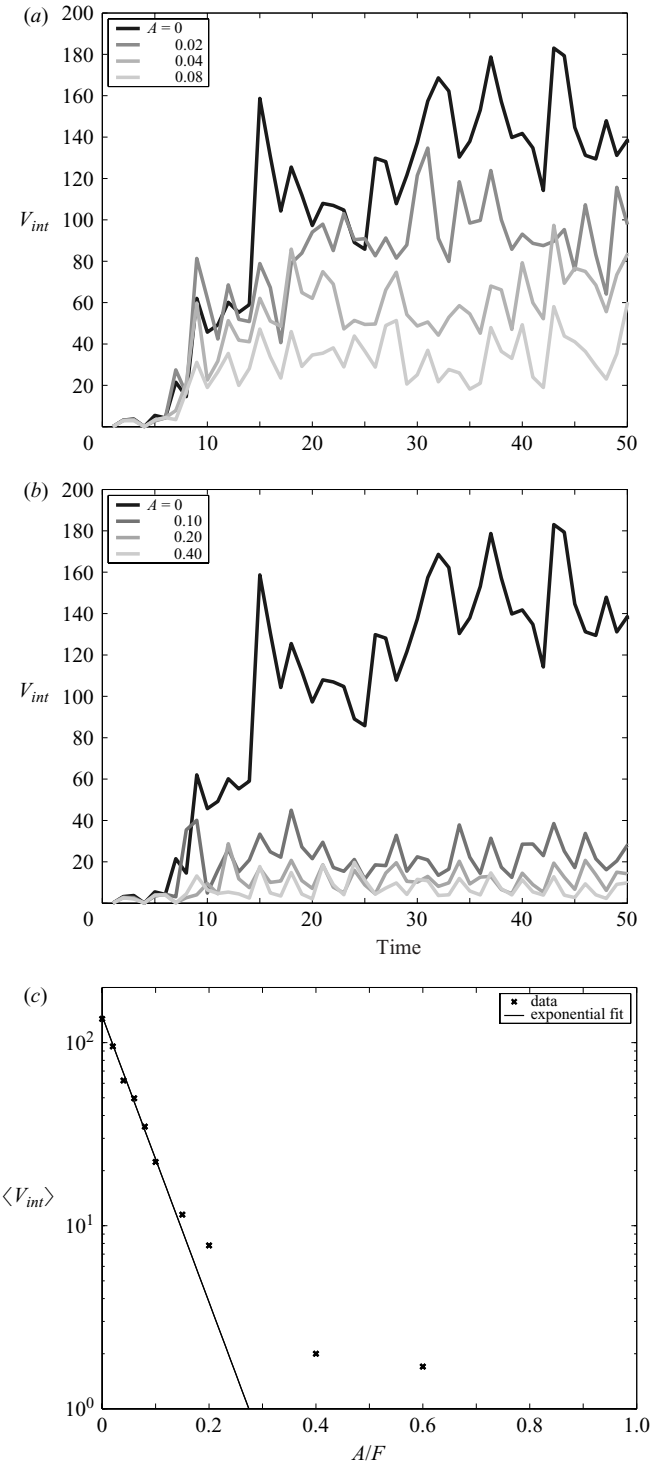

FIGURE 16. Time evolution of $V_{int}(t)$ and the average interior enstrophy $\overline{V}_{int}$ for numerical simulations with $Re = 15\,000$. (*a*) $V_{int}(t)$ for $\mathscr{A}/\mathscr{F} = 0$, $\mathscr{A}/\mathscr{F} = 0.02$, $\mathscr{A}/\mathscr{F} = 0.04$, and $\mathscr{A}/\mathscr{F} = 0.08$. (*b*) Data for $\mathscr{A}/\mathscr{F} = 0$ (for reference), $\mathscr{A}/\mathscr{F} = 0.10$, $\mathscr{A}/\mathscr{F} = 0.20$, and $\mathscr{A}/\mathscr{F} = 0.40$. In (*c*) the average interior enstrophy $\overline{V}_{int}$ is plotted as function of $\mathscr{A}/\mathscr{F}$, and can be seen to decrease exponentially for $0 < \mathscr{A}/\mathscr{F} < 0.2$.

Run	$\mathscr{A}$	$\lvert\omega_{mean}\rvert$	ρ_{mean}/L
1	0.00	25.4	0.130
2	0.02	23.9	0.137
3	0.04	19.2	0.143
4	0.06	19.8	0.144
5	0.08	18.1	0.148
6	0.10	16.7	0.154
7	0.15	17.8	0.173
8	0.20	12.4	0.196
9	0.40	6.75	0.285
10	0.60	1.21	0.433

TABLE 4. A summary of the parameters used in the simulations with Ekman damping (with $Re = 15\,000$ and $\mathscr{F} = 1.00$). The last two columns represent the dimensionless mean vortex amplitude, $|\omega_{mean}|$, and the average vortex radius, ρ_{mean}/L, respectively.

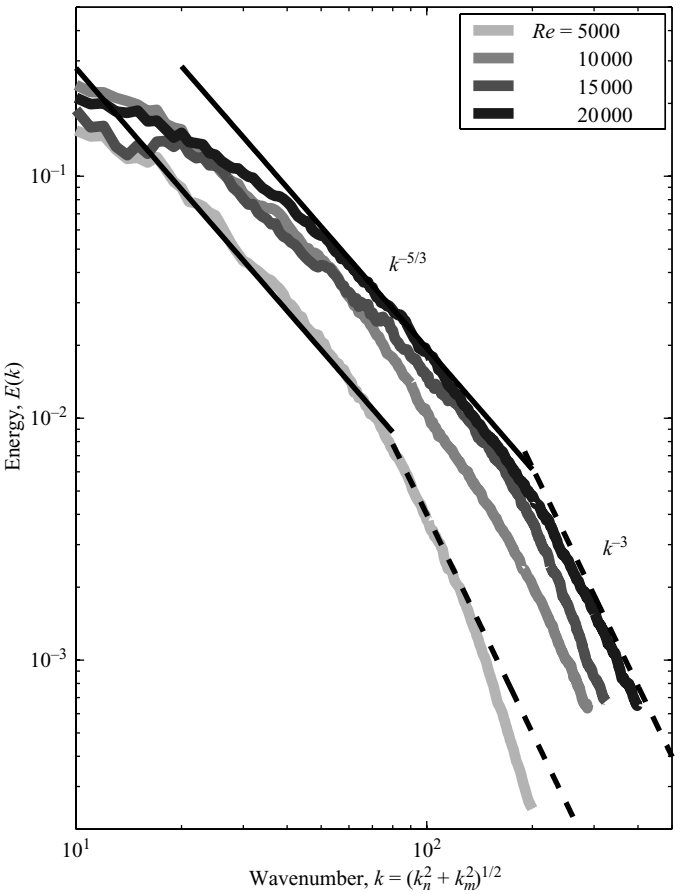

FIGURE 17. A log–log graph of the phase averaged energy spectrum for $Re = 5000$, 10 000, 15 000 and 20 000 and $\mathscr{F} = 0.80$ (runs 27, 34, 39 and 42, respectively, in table 3) at $t = 30$. For both values of Re, a $k^{-5/3}$ power law for low wavenumbers, and a k^{-3} power-law fit exists for high wavenumbers. These power laws are consistent with an inverse energy cascade, and an enstrophy cascade, respectively. Also note the shift of the 'knee' in these spectra as the Reynolds number changes, consistent with changes in boundary-layer thickness.

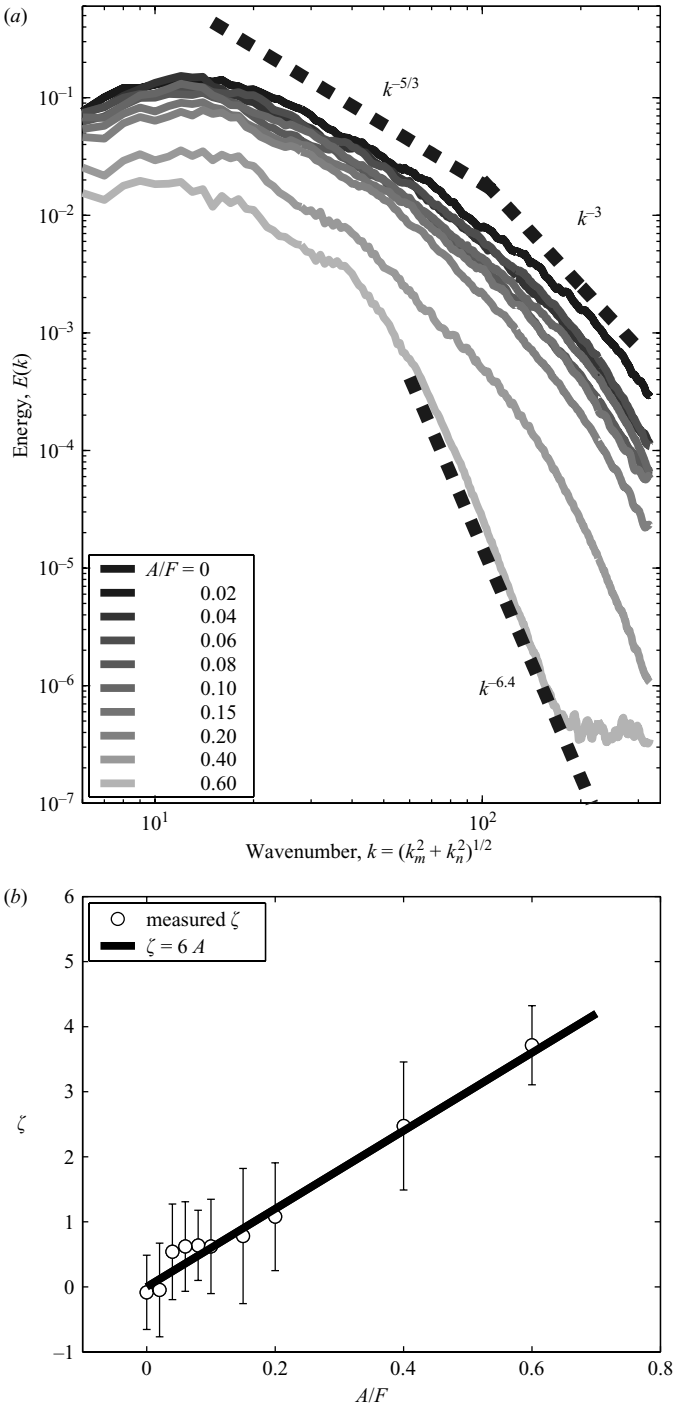

FIGURE 18. (*a*) A log–log graph of the (phase averaged) energy spectrum for the different values of $\mathscr{A}/\mathscr{F}$ (0, 0.04, 0.06, 0.10, 0.20 and 0.60) for $Re = 15\,000$ and $\mathscr{F} = 1.00$ at $t = 30$. As the value of $\mathscr{A}/\mathscr{F}$ increases, and the flow becomes more strongly damped, the spectra become steeper. Strong damping appears to suppress the formation of any vortices and the flow is not turbulent. For weak damping the spectra are consistent with a $k^{-5/3}$ power law for low wavenumbers, and a $k^{-3-\zeta}$ power law for high wavenumbers, with $\zeta \approx (6 \pm 1)\mathscr{A}$. (*b*) The scaling exponent ζ of the spectrum in the direct cascade regime for different values of $\mathscr{A}/\mathscr{F}$.

$k^{-5/3}$ and $k^{-3-\zeta}$ spectrum are present (with ζ proportional to $\mathscr{A}$ and in the range $0 < \zeta < 1$). The spectra steepen with increasing $\mathscr{A}$ at high wavenumbers. The first three simulations, with $\mathscr{A}/\mathscr{F} = 0.00$, 0.04 and 0.06, revealed spectra with a $k^{-5/3}$ range for $30 < k < 140$ and a $k^{-3-\zeta}$ range for $160 < k < 300$ where ζ is slowly increasing from 0 to 0.3–0.4. The more strongly damped cases with $\mathscr{A}/\mathscr{F} = 0.10$ and 0.20 show an overall decrease in energy, but similar spectra are observed with a $k^{-3.5}$ and k^{-4} spectrum for high wavenumbers, respectively. Increasing the Ekman damping further, we find that the simulations with $\mathscr{A}/\mathscr{F} = 0.40$ and 0.60 show much steeper (and most probably exponentially decaying) spectra. In particular when $\mathscr{A}/\mathscr{F} = 0.60$, the flow field is not turbulent anymore and vorticity is mainly present in thin boundary layers, which do not detach from the boundary (and do not roll up to form vortices).

The spectral slope, for $k \gtrsim 140$ (for small $\mathscr{A}$) and for $k \gtrsim 100$ (for relatively large $\mathscr{A}$), as a function of the dimensionless Ekman damping rate $\mathscr{A}$ is plotted in figure 18(*b*). The following modified power law is found: $k^{-3-\beta\mathscr{A}}$ with $\beta = 6 \pm 1$ (note that $\mathscr{F} = 1.0$ for this set of simulations). The steepening of the high wavenumber spectrum with increasing drag has been observed in laboratory experiments using magnetically forced stratified flows (Danilov *et al.* 2002; Boffetta *et al.* 2005), in rotating flows (Narimousa, Maxworthy & Spedding 1991) and in decaying turbulence in thin soap films (Kellay, Wu & Goldburg 1998) where the high-wavenumber spectrum had slopes from k^{-3} to $k^{-5.5}$. Both Bernard (2000) and Nam *et al.* (2000) studied the influence of friction on the direct cascade of forced two-dimensional turbulence and showed that the k^{-3}-scaling of the direct enstrophy cascade had to be corrected by a factor proportional to the friction $\mathscr{A}$, i.e. the following scaling is expected: $k^{-3-\zeta}$ with $\zeta = \beta\mathscr{A} > 0$. Numerical confirmation was provided by Nam *et al.* (2000) and Boffetta *et al.* (2002) with direct numerical simulation (DNS) of Ekman–Navier–Stokes turbulence, and their results are consistent with our numerical data. Nam *et al.* (2000) obtained $\beta \approx 5$ and Boffetta *et al.* (2002) found the value $\beta \approx 9$.

It is interesting to compare these numerical observations with the energy and passive scalar spectra that were obtained in the laboratory experiments discussed in § 3.2. The wavenumber at which the transition occurs between the $k^{-5/3}$ and k^{-3} power laws is at a similar wavenumber to the maximum that could be resolved using particle-tracking velocimetry in the laboratory experiments (where $Re \sim 15\,000$). Hence, it was not surprising that we could not resolve a k^{-3} power law in these laboratory experiments. The observed k^{-1} power law spectrum of the scalar spectrum (figure 8) is in the same high-wavenumber range in which the enstrophy cascade is observed in these numerical experiments, in agreement with theory and simulations of Nam *et al.* (1999, 2000). They noted that at high wavenumbers the straining of filaments of vorticity is essentially the same as that of a passive scalar. As the energy spectrum is related to the enstrophy spectrum by $V(k) \sim k^2 E(k)$, the enstrophy spectrum (and the spectra of passive tracers) should have a k^{-1} spectrum when the energy spectrum shows a k^{-3} range at high wavenumbers.

5. Conclusion

We have conducted experiments and numerical simulations of a quasi-two-dimensional forced flow where the boundary layers near the lateral no-slip walls act as the sole source of vorticity. These experiments and simulations extend conclusions from previous observations on energy spectra of decaying two-dimensional turbulence in bounded domains with no-slip walls (Clercx & van Heijst 2000) to those of forced (although presumably not fully turbulent) two-dimensional bounded flows. The 'knee' in the energy spectrum, at the border between the $k^{-5/3}$ and the k^{-3} range, is

determined by the boundary-layer thickness. Moreover, the present experimental set-up enables the generation of a sea of interacting vortices with specific characteristics, such as the average vortex radius and strength which are determined by the forcing parameters.

The average vortex size in the present experiments is controlled by the boundary-layer thickness and the 'roll-up' process of these layers. The scaling is described by equation (2.6), and shows good agreement with the data from numerical simulations. Agreement is also found with laboratory experiments where vortex sizes corresponding to approximately 10–15 % of the tank size were observed for $Re = 15\,000$ and $0.5 \lesssim \mathscr{F} \lesssim 2.0$. The scaling of the average vortex amplitude is found to agree with equation (2.7).

There are two main reasons why subsequent vortex interactions do not lead to the emergence of larger structures, namely vortex stripping by the background shear and decay by Ekman pumping. Numerical experiments by Boffetta *et al.* (2002) have shown that Ekman pumping can limit the size of vortices in continually forced two-dimensional turbulence, so it is difficult to distinguish between the two processes in a laboratory experiment. In the absence of Ekman pumping, numerical simulations have clearly shown that vortex stripping is the important mechanism by which the eddy size is limited. Numerical simulations using a linear damping term to model the Ekman decay revealed that, for a forcing frequency $\mathscr{A}/\mathscr{F} \lesssim 0.1$, there was little change to the vortex size and energy spectrum compared to the undamped case. For $\mathscr{A}/\mathscr{F} \gtrsim 0.3$, the vorticity formed at the boundaries decays rapidly before it is injected into the interior and hence no turbulent field emerges. Laboratory experiments typically lie in the range of $\alpha/f = 0.04$–0.16, so that vortex stripping was a more important mechanism than Ekman damping for removing vorticity from the coherent vortex structures.

In both numerical and laboratory experiments, we found that the degree of turbulence within the tank is determined by the frequency and amplitude of the forcing. When $\mathscr{F} \lesssim 1.5$, the interior becomes well mixed by a field of dipoles resulting from flow separation. When $\mathscr{F} \gtrsim 2.0$, the flow is not turbulent because the tank oscillates too fast for the formation of dipolar structures to occur, so that any vortices formed remain near the walls. For these weakly turbulent cases there is a strong difference in mixing rates between the centre of the tank (where dispersion is very slow) and the near-wall region, where dispersion occurs rapidly along the periphery of the tank.

Energy spectra calculated for numerical simulations with $Re = 5000$, 10 000, 15 000 and 20 000 with $\mathscr{F} = 0.80$ revealed two distinct parts of the spectrum above and below the characteristic wavenumber of the boundary layer, k_δ. For $k < k_\delta$, the spectrum obeyed a $k^{-5/3}$ power law, which is usually thought of as characterizing an inverse energy cascade. For $k > k_\delta$, the spectrum had a steeper k^{-3} power law, representative for decay of enstrophy by filamentation of vorticity. Because k_δ is proportional to $\sqrt{Re}$, by varying Re in the simulations (and keeping $\mathscr{F}$ constant) we were able to change the wavenumber at which energy is injected into the flow. When a linear damping term was included to model the effect of Ekman pumping, the spectra were generally steeper than in the non-damped case, but for the parameter range relevant for the laboratory experiments it was found that both a $k^{-5/3}$ and a k^{-3}-to-$k^{-3.5}$ range should be present in the energy spectrum. The high-wavenumber spectrum in our numerical simulations seems consistent with theoretical predictions by Bernard (2000) and Nam *et al.* (2000), who showed that the direct cascade is characterized by a power law: $k^{-3-\zeta}$, with $\zeta \propto \mathscr{A}$. The constant of proportionality is in the same range as previously reported by Nam *et al.* (2000) and Boffetta *et al.* (2002).

In the laboratory experiments we observed a $k^{-5/3}$ power law of the energy spectrum (the k^{-3} range could not be resolved directly). The intensity spectrum

of the dye, after having been mixed by the turbulent field, had a k^{-1} power law behaviour at high wavenumbers, consistent with the prediction of Batchelor (1959). The laboratory observations of a k^{-1} scalar spectrum are consistent, although not a sufficient condition, with the presence of the k^{-3} enstrophy cascade (Nam *et al.* 1999).

We would like to thank David Molenaar, Ruben Trieling and Ted Sheppard for helpful discussions, Ad Holten and Gert van der Plas for technical assistance in the laboratory, and Andrew Kiss and John Wettlaufer for careful reading of the manuscript. Part of this paper was written while M. G. W. was employed at the Department of Geology and Geophysics at Yale University, and their financial support is gratefully acknowledged.

REFERENCES

Bastiaans, R. J. M., van der Plas, G. A. J. & Kieft, R. N. 2002 The performance of a new PTV algorithm applied in super-resolution PIV. *Exps. Fluids* **32**, 346–356.

Batchelor, G. K. 1959 Small-scale variation of convected quantities like temperature in turbulent fluid. Part 1. General discussion and the case of small conductivity. *J. Fluid Mech.* **5**, 113–133.

Bernard, D. 2000 Influence of friction on the direct cascade of the 2D forced turbulence. *Europhys. Lett.* **50**, 333–339.

Boffetta, G., Celani, A., Musacchio, S. & Vergassola, M. 2002 Intermittency in two-dimensional Ekman–Navier–Stokes turbulence. *Phys. Rev.* E **66**, 026304.

Boffetta, G., Cenedese, A., Espa, S. & Musacchio, S. 2005 Effects of friction on 2D turbulence: an experimental study of the direct cascade. *Europhys. Lett.* **71**, 590–596.

Clercx, H. J. H. 1997 A spectral solver for the Navier–Stokes equations in the velocity–vorticity formulation for flows with two non-periodic directions. *J. Comput. Phys.* **137**, 186–211.

Clercx, H. J. H. & van Heijst, G. J. F. 2000 Energy spectra for decaying two-dimensional turbulence in a bounded domain. *Phys. Rev. Lett.* **85**, 306–309.

Danilov, S., Dolzhanskii, F. V., Dovzhenko, V. A. & Krymov, V. A. 2002 Experiments on free decay of quasi-two-dimensional turbulent flows. *Phys. Rev.* E **65**, 036316.

Dritschel, D. G. & Zabusky, N. J. 1996 On the nature of vortex interactions and models in unforced nearly-inviscid two-dimensional turbulence. *Phys. Fluids* **8**, 1252–1256.

van Heijst, G. J. F. 1989 Spin-up phenomena in non-axisymmetric containers. *J. Fluid Mech.* **206**, 171–191.

van Heijst, G. J. F., Davies, P. A. & Davis, R. G. 1990 Spin-up in a rectangular container. *Phys. Fluids* A **2**, 150–159.

Kellay, H., Wu, X. L. & Goldburg, W. I. 1998 Vorticity measurements in turbulent soap films. *Phys. Rev. Lett.* **80**, 277–280.

van de Konijnenberg, J. A., Andersson, H. I., Billdal, J. T. & van Heijst, G. J. F. 1994 Spin-up in a rectangular tank with low angular velocity. *Phys. Fluids* **6**, 1168–1176.

Kundu, P. K. 1990 *Fluid Mechanics*. Academic.

Mariotti, A., Legras, B. & Dritschel, D. G. 1994 Vortex stripping and the erosion of coherent structures in two-dimensional flows. *Phys. Fluids* **6**, 3954–3962.

Nam, K., Guzdar, P. N., Antonsen, T. M. & Ott, E. 1999 K-spectrum of finite lifetime passive scalars in Lagrangian chaotic fluid flows. *Phys. Rev. Lett.* **83**, 3426–3429.

Nam, K., Ott, E., Antonsen, T. M. & Guzdar, P. N. 2000 Lagrangian chaos and the effect of drag on the enstrophy cascade in two-dimensional turbulence. *Phys. Rev. Lett.* **84**, 5134–5136.

Narimousa, S., Maxworthy, T. & Spedding, G. R. 1991 Experiments on the structure and dynamics of forced, quasi-two-dimensional turbulence. *J. Fluid Mech.* **223**, 113–133.

Okubo, A. 1970 Horizontal dispersion of floatable particles in the vicinity of velocity singularities such as convergences. *Deep-Sea Res.* **17**, 445–454.

Pedlosky, J. 1987 *Geophysical Fluid Dynamics*. Springer.

Trieling, R. R., Beckers, M. & van Heijst, G. J. F. 1997 Dynamics of monopolar vortices in a strain flow. *J. Fluid Mech.* **345**, 165–201.

Weiss, J. B. 1991 The dynamics of enstrophy transfer in two-dimensional hydrodynamics. *Physica* D **48**, 273–294.